Attosecond Photoelectron Metrology: from light to electrons

Ammitzböll, Mattias

2025

Document Version:
Publisher's PDF, also known as Version of record

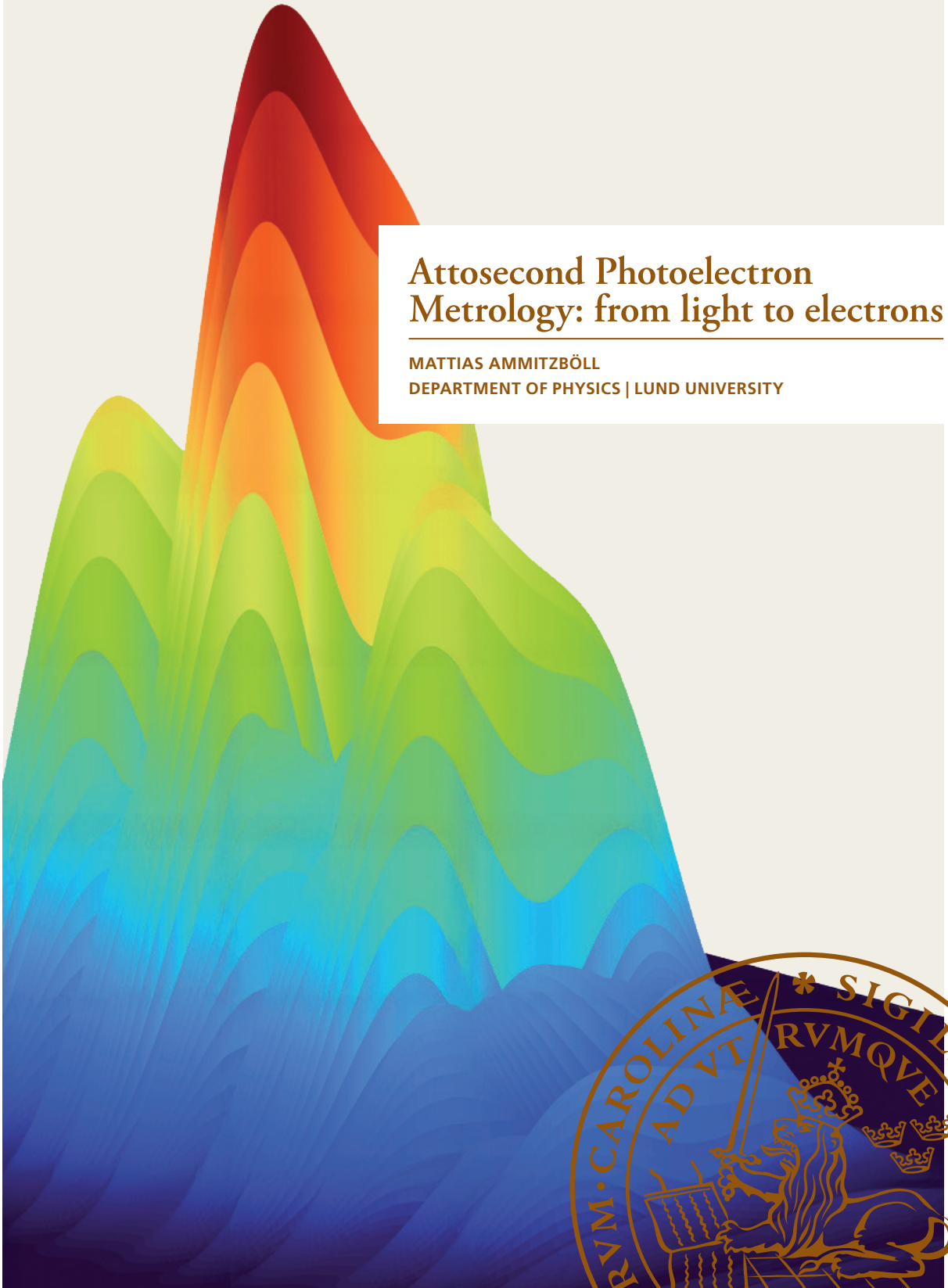

Attosecond Photoelectron Metrology: from light to electrons

MATTIAS AMMITZBÖLL
DEPARTMENT OF PHYSICS | LUND UNIVERSITY

Printed by Media-Tryck, Lund 2025 NORDIC SWAN ECOLABEL 3041 0903

LUND UNIVERSITY

Faculty of Engineering, LTH
Department of Physics

Lund Reports on Atomic Physics, LRAP617(2025)
ISBN 978-91-8104-636-6
ISSN 0281-2762

Attosecond Photoelectron Metrology: from light to electrons

Attosecond Photoelectron Metrology: from light to electrons

by Mattias Ammitzböll

LUND
UNIVERSITY

Thesis for the degree of PhD in Physics
Thesis advisors: Prof. Anne L'Huillier, Dr. Cord Arnold, Dr. Mathieu Gisselbrecht and Dr. David Busto.
Faculty opponent: Prof. Charles Bourassin-Bouchet

To be presented, with the permission of the Faculty of Engineering, LTH of Lund University, for public criticism in Rydberg lecture hall at the Department of Physics on Friday, the 26th of September 2025 at 09:15.

Organization
LUND UNIVERSITY

Department of Physics
Box 118
SE–221 00 LUND
Sweden

Document name
DOCTORAL DISSERTATION

Date of disputation
2025-09-26

Sponsoring organization

Author(s)
Mattias Ammitzböll

Title and subtitle
Attosecond Photoelectron Metrology: from light to electrons

Abstract
The interaction between Extreme UltraViolet (XUV) Attosecond Pulse Trains (APT) and matter enables real-time investigation of electron dynamics on their natural time-scale. This is achieved by the addition of a weak InfraRed (IR) field, which probes the ionization process. However, achieving the required temporal and spectral precision for such studies imposes stringent demands on the experimental setup. This thesis presents the development and implementation of a novel, ultra-stable, and flexible Mach-Zehnder interferometer for attosecond photoelectron metrology. The setup features active stabilization achieving < 13 attoseconds (RMS) temporal jitter and enables photoelectron spectroscopy with an energy-resolution better than 80 meV for low-energy electrons.

Using this setup, two complementary experimental schemes have been employed. First, resonant two-photon ionization processes are investigated using the Reconstruction of Attosecond Beating By Interference of Two-photon transitions (RABBIT) protocol. In helium, we measure phase variations as functions of angle and energy across the 3p, 4p, and 5p Rydberg series. Angular channel selection is achieved using cross-polarized pump and probe fields. In argon, we study the $3s^{-1}4p$ Fano resonance, resolving the spin-orbit (SO) splitting and observing phase variations that depend on the spectral width of the XUV pulse. These effects are interpreted by taking into account the influence of final-state interactions.

Second, a new quantum state tomography protocol, KRAKEN (a Swedish acronym for *Kvanttillstånds tomogRafi av AttoseKund ElektroNvågpaket*), is introduced and experimentally demonstrated. KRAKEN enables the reconstruction of the photoelectron density matrix, extending attosecond metrology to partially coherent or mixed quantum states. We show good agreement between KRAKEN measurements and theoretical predictions for photoionization in helium and argon. The protocol is further extended with a poly-chromatic probe scheme (Poly-KRAKEN), which improves the efficiency and reduces the duration of the experimental measurement by exploiting both spectral and temporal domains simultaneously.

Key words
Attosecond, Photoionization, Quantum state tomography

Classification system and/or index terms (if any)

Supplementary bibliographical information

Language
English

ISSN and key title
0281-2762

ISBN
978-91-8104-636-6 (print)
978-91-8104-637-3 (pdf)

Recipient's notes

Number of pages
208

Price

Security classification

Signature _____ Date 2025-08-13

Attosecond Photoelectron Metrology: from light to electrons

by Mattias Ammitzböll

LUND
UNIVERSITY

A doctoral thesis at a university in Sweden takes either the form of a single, cohesive research study (monograph) or a summary of research papers (compilation thesis), which the doctoral student has written alone or together with one or several other author(s).

In the latter case the thesis consists of two parts. An introductory text puts the research work into context and summarizes the main points of the papers. Then, the research publications themselves are reproduced, together with a description of the individual contributions of the authors. The research papers may either have been already published or are manuscripts at various stages (in press, submitted, or in draft).

Cover illustration front: The photoelectron spectrum as a function of delay, simulated in helium using the Poly-KRAKEN protocol.

Cover illustration back: A photo after our first successful RABBIT measurement after the experimental upgrade detailed in **Paper I** . The people shown in the photo (from left to right) are: Sizuo Luo, Anne L'Huillier, Robin Weissenbilder, Mattias Ammitzböll (me), Hugo Laurell, and Cord Arnold.

Use of Artificial Intelligence: Certain aspects of the writing and text refinement of this thesis were assisted by generative language models. The final interpretation, analysis, and conclusions presented in this work remain the sole responsibility of the author.

Funding information: The thesis work was financially supported by the Wallenberg Centre for Quantum Technology (WACQT).

Faculty of Engineering, LTH, Department of Physics

ISBN: 978-91-8104-636-6 (print)
ISBN: 978-91-8104-637-3 (pdf)
ISSN: 0281-2762
Lund Reports on Atomic Physics, LRAP617(2025)

Printed in Sweden by Media-Tryck, Lund University, Lund 2025

Media-Tryck is a Nordic Swan Ecolabel certified provider of printed material. Read more about our environmental work at www.mediatryck.lu.se

MADE IN SWEDEN

"To see a World in a Grain of Sand
And a Heaven in a Wild Flower,
Hold Infinity in the Palm of Your Hand
And Eternity in an Hour. "

- William Blake

Abstract

The interaction between Extreme UltraViolet (XUV) Attosecond Pulse Trains (APT) and matter enables real-time investigation of electron dynamics on their natural timescale. This is achieved by the addition of a weak InfraRed (IR) field, which probes the ionization process. However, achieving the required temporal and spectral precision for such studies imposes stringent demands on the experimental setup. This thesis presents the development and implementation of a novel, ultra-stable, and flexible Mach-Zehnder interferometer for attosecond photoelectron metrology. The setup features active stabilization achieving < 13 attoseconds (RMS) temporal jitter and enables photoelectron spectroscopy with an energy-resolution better than 80 meV for low-energy electrons.

Using this setup, two complementary experimental schemes have been employed. First, resonant two-photon ionization processes are investigated using the Reconstruction of Attosecond Beating By Interference of Two-photon transitions (RABBIT) protocol. In helium, we measure phase variations as functions of angle and energy across the 3p, 4p, and 5p Rydberg series. Angular channel selection is achieved using cross-polarized pump and probe fields. In argon, we study the $3s^{-1}4p$ Fano resonance, resolving the spin-orbit (SO) splitting and observing phase variations that depend on the spectral width of the XUV pulse. These effects are interpreted by taking into account the influence of final-state interactions.

Second, a new quantum state tomography protocol, KRAKEN (a Swedish acronym for *Kvanttillstånds tomogRafi av AttoseKund ElektroNvågpaket*), is introduced and experimentally demonstrated. KRAKEN enables the reconstruction of the photoelectron density matrix, extending attosecond metrology to partially coherent or mixed quantum states. We show good agreement between KRAKEN measurements and theoretical predictions for photoionization in helium and argon. The protocol is further extended with a poly-chromatic probe scheme (Poly-KRAKEN), which improves the efficiency and reduces the duration of the experimental measurement by exploiting both spectral and temporal domains simultaneously.

Popular Science Summary

Attosecond Photoelectron Metrology: from light to electrons, is the title I have chosen for this thesis. With it, I hope to guide the curious reader through the work we have done. However, just as I would have felt at the start of my PhD, this title may seem a bit hard to decipher at first glance. If you feel the same, or if you would prefer to begin this journey in a more accessible way, then this section is for you.

In our group, we aim to study the movements and interactions involved with *electrons*. These phenomena are not governed by the laws of "classical physics", but are instead governed by quantum mechanics. To be able to resolve these phenomena, one would need a "stopwatch" with a finer precision than the duration of these phenomena. As for electrons, their natural timescale is on the scale of *attoseconds* (1 as = 10^{-18} s). There are as many attoseconds in a single second, as there have been seconds since the Big Bang. Naturally, we do not have cameras or electronics that work on this timescale, quite frankly not even close. So in order to study these movements and interactions, we must do something else.

Similar to the quick and intense flash of an analog camera, people have discovered a way to generate very short *light* pulses that may resolve the electrons on their natural timescale. As described in the beginning of the thesis, these ultrafast light pulses are generated by focusing a state-of-the-art laser into a gas. In these extreme, high-intensity conditions, a strange phenomenon known as High-order Harmonic Generation (HHG) may occur. Light may be generated with new frequencies that are multiples of the generating laser frequency, known as harmonics. Much like with a string instrument, one may generate the fourth harmonic overtone of the sound frequency, by clamping the string to a fourth of its original length. Similarly to the string instrument, in HHG several harmonic frequencies are generated. Where the interference of these harmonics leads to the generation of an *Attosecond Pulse Train (APT)*, a series of light pulses, each with a much shorter duration than that of the ultrafast laser that generates them.

With these attosecond pulses we have our needed "stopwatch", but the question remains of how we can perform the experiments and retrieve the relevant data. As explained by Albert Einstein himself a little more than a hundred years ago [1], light with sufficiently high frequencies may be able to liberate the bound electrons. If the APT is focused into a gas, the free electrons generated are known as *photoelectrons* since they are set free by a light-matter interaction with light quanta, known as photons. The higher the frequency of the harmonic that liberated the electron, the higher the kinetic energy of the photoelectron ejected is found to be.

Which brings us to the last part of the title, *metrology*, the scientific study of mea-

surement. Methods developed and covered in this thesis can be summed down to essentially two different techniques. In the first experiment, we study the interference between photoelectrons that are generated by the absorption of light with different harmonic frequencies. Here we are able to extract both wave properties of the light and an insight into the atomic structure. If we go back to the music analogy, this method would be similar to if we try to study if two musicians playing different harmonic overtones are able to play ”in phase” with each other or not. In the second experiment, we instead study the interference between photoelectrons that are generated by the absorption of light within a single harmonic frequency. Here we are able to extract quantum properties of the photoelectron wave-packet created. In the analogy, this would be more like studying the degree to which two or more musicians are playing ”in phase” with each other within the same harmonic overtone.

Populärvetenskaplig sammanfattning

Attosekundsfotoelektronmetrologi: från ljus till elektroner är titeln jag har valt för denna avhandling. Genom den hoppas jag kunna guida den nyfikna läsaren genom det arbete vi har utfört. Men, precis som jag själv kände i början av min doktorandtid, kan denna titel initialt verka något svår att tyda. Om du känner likadant, eller om du föredrar att påbörja denna resa på ett mer lättillgängligt sätt, så är detta avsnitt för dig.

I vår forskargrupp försöker vi att studera rörelser och interaktioner som involverar *elektroner*. Dessa fenomen styrs inte av den klassiska fysikens lagar, utan av kvantmekanikens. För att kunna observera dem krävs ett ”stoppur” med bättre tidsupplösning än själva fenomenens tidsförlopp. Elektroners naturliga tidsskala är i storleksordningen *attosekunder* (1 as = 10^{-18} s). Det finns lika många attosekunder i en enda sekund som det har funnits sekunder sedan Big Bang. Naturligtvis har vi varken kameror eller elektronik som fungerar på denna tidsskala, faktiskt inte ens i närheten. Så för att studera dessa rörelser och interaktioner måste vi ta till en annan metod.

På ett liknande sätt som den snabba och intensiva blixten i en analog kamera, har forskare upptäckt ett sätt att generera mycket korta *ljuspulser* som kan upplösa elektronernas rörelser på deras naturliga tidsskala. Som beskrivs i början av denna avhandling, genereras dessa ultrasnabba ljuspulser genom att fokusera en toppmodern laser in i en gas. Under dessa extrema, högintensiva förhållanden kan ett märkligt fenomen uppstå, så kallat övertonsgenerering (*High-order Harmonic Generation, HHG)*. Vid dessa förhållanden kan ljus genereras med nya frekvenser som är multiplar av den ursprungliga laserfrekvensen, så kallade övertoner eller harmoniska frekvenser. Ungefär som på ett stränginstrument, där man kan skapa den fjärde övertonen genom att korta strängen till en fjärdedel av dess längd, genereras flera olika övertonsfrekvenser i HHG. Interferensen mellan dessa frekvenser leder till skapandet av ett *AttosekundsPulsTåg (APT)*, en serie ljuspulser, där varje puls är mycket kortare än den redan ultrasnabba laserpuls som genererade dem.

Med dessa attosekundspulser har vi vårt nödvändiga ”stoppur”, men frågan kvarstår: hur utför vi experimenten och får ut den relevanta informationen? Som Albert Einstein förklarade för lite mer än hundra år sedan [1], kan ljus med frekvenser med tillräckligt hög energi frigöra bundna elektroner. Om vi fokuserar en APT in i en gas, genereras fria elektroner som kallas *fotoelektroner*, eftersom de frigörs genom ljus–materia-interaktion med ljuskvanta, så kallade fotoner. Ju högre frekvens den överton som frigjorde elektronen hade, desto högre kinetisk energi får den utsända fotoelektronen.

Detta för oss till den sista delen av titeln, *metrologi*, den vetenskapliga studien av mätningar. Metoderna som har utvecklats och behandlas i denna avhandling kan i hu-

vudsak delas upp i två olika tekniker. I det första experimentet studerar vi interferens mellan fotoelektroner som genererats genom absorption av ljus med olika övertonsfrekvenser. Här kan vi extrahera både ljusets vågegenskaper och få insikt i atomstrukturen. Om vi återvänder till musikanalogin, skulle denna metod motsvara att studera om två musiker som spelar olika övertoner spelar ”i fas” med varandra eller inte. I det andra experimentet studerar vi istället interferens mellan fotoelektroner som genererats genom absorption av ljus inom en och samma övertonsfrekvens. Här kan vi extrahera kvantegenskaper hos det skapade fotoelektronvågpaketet. I analogin skulle detta motsvara att analysera i vilken utsträckning två eller fler musiker är i fas med varandra när de spelar inom samma överton.

List of publications

This thesis is based on the following publications, referred to by their Roman numerals:

I **Ultra-stable and versatile high-energy resolution setup for attosecond photoelectron spectroscopy**
S. Luo, R. Weissenbilder, H. Laurell, **M. Ammitzböll**, V. Poulain, D. Busto, L. Neoričić, C. Guo, S. Zhong, D. Kroon, R. J. Squibb, R. Feifel, M. Gisselbrecht, A. L'Huillier and C. L. Arnold
Advances in Physics: X, **8** 1 , pp. 1-23, (2023)

II **Influence of final state interactions in attosecond photoelectron interferometry**
S. Luo, R. Weissenbilder, H. Laurell, R. Y. Bello, C. Marante, **M. Ammitzböll**, L. Neoričić, A. Ljungdahl, R. J. Squibb, R. Feifel, M. Gisselbrecht, C. L. Arnold, F. Martín, E. Lindroth, L. Argenti, D. Busto and A. L'Huillier
Physical Review Research, **6**:043271, (2024)

III **Resonant two-photon ionization of helium atoms studied by attosecond interferometry**
L. Neoričić, D. Busto, H. Laurell, R. Weissenbilder, **M. Ammitzböll**, S. Luo, J. Peschel, H. Wikmark, J. Lahl, S. Maclot, R. J. Squibb, S. Zhong, P. Eng-Johnsson, C. L. Arnold, M. Gisselbrecht, E. Lindroth and A. L'Huillier
Frontiers in Physics, **10**, (2022)

IV **Continuous-variable quantum state tomography of photoelectrons**
H. Laurell, D. Finkelstein-Shapiro, C. Dittel, C. Guo, R. Demjaha, **M. Ammitzböll**, R. Weissenbilder, L. Neoričić, S. Luo, M. Gisselbrecht, A. Buchleitner, T. Pullerits, A. L'Huillier and D. Busto
Physical Review Research, **4**: 033220, (2022)

V **Measuring the quantum state of photoelectrons**

H. Laurell, S. Luo, R. Weissenbilder, **M. Ammitzböll**, S. Ahmed, H. Söderberg, C. L. M. Petersson, V. Poulain, C. Guo, C. Dittel, D. Finkelstein-Shapiro, R. J. Squibb, R. Feifel, M. Gisselbrecht, C. L. Arnold, A. Buchleitner, E. Lindroth, A. Frisk Kockum, A. L'Huillier and D. Busto
Nature Photonics, **19**, pp.352-357, (2025)

VI **Towards quantum-state tomography of photoelectrons using spectral Golomb rulers**
M. Ammitzböll, E. Boati, G. Arvidsson, R. Weissenbilder, M. Li, H. Wang, S. Eklund, H. Laurell, C. Dittel, M. Canhota, C. Lévêque, J. Dubois, R. J. Squibb, R. Feifel, M. Gisselbrecht, C. L. Arnold, R. Taïb, J. Caillat, A. L'Huillier, S. Luo and D. Busto
Manuscript, (2025)

Appendix

VII **A single-shot dispersion-scan based on a grism**

D. Díaz Rivas, I. Sytcevich, M. Canhota, C. Guo, **M. Ammitzböll**, E. A. Boati, M. Miranda, A. L'Huillier, A. Viotti and C. L. Arnold
Submitted, (2025)

Abbreviations

1/2/3D	One/Two/Three Dimensional
AOPDF	Acousto-Optical Programmable Dispersive Filter
APT	Attosecond Pulse Train
CC	Continuum-Continuum
CPA	Chirped Pulse Amplification
CW	Continuous Wave
FROG	Frequency-Resolved Optical Gating
FTL	Fourier Transform Limited
FWHM	Full Width at Half Maximum
HHG	High-order Harmonic Generation
HOWP	High-Order WavePlate
IR	InfraRed
KLM	Kerr Lens Mode-locking
KRAKEN	quantum state tomography of attosecond electron wave-packets
MBES	Magnetic Bottle Electron Spectrometer
MCP	MicroChannel Plate
QST	Quantum State Tomography
RABBIT	Reconstruction of Attosecond Beating By Interference of Two-photon transitions
RMS	Root Mean Square
RPAE	Random Phase Approximation with Exchange
RRPAE	Relativistic Random Phase Approximation with Exchange
SB	SideBand
SO	Spin-Orbit
Ti:Sa	Titanium:Sapphire
ToF	Time-of-Flight
TSM	Three-Step Model
VMIS	Velocity Map Imaging Spectrometer
XUV	Extreme UltraViolet

Contents

Part I

Thesis

Chapter 1

Introduction

1.1 A brief background to this thesis

One of the foundational phenomena in light-matter interaction, first discovered by Heinrich Hertz in 1887 [2], is the *photoelectric effect*. This phenomenon, as explained by Albert Einstein [1] (later earning him a Nobel prize), occurs when high-frequency light is absorbed by an atom, molecule, or solid, causing one or more electrons to be emitted. The atom, molecule, or solid is only photoionized if the photon energy $\hbar\Omega$ overcomes the electron binding energy I_p. If so, the photoelectron is emitted into the continuum with the kinetic energy $\epsilon_f = \hbar\Omega - I_p$. By studying the kinetic energy of the photoelectron, detailed information about the internal structure of matter can be obtained. This technique is known as *photoelectron spectroscopy*, developed by Kaj Siegbahn in 1956, earning him a Nobel prize [3].

Photoelectron spectroscopy gives an incomplete description of the process of photoionization and the properties of the photoelectron. From the cross-section only, proportional to the probability that a photoelectron is emitted with a certain kinetic energy, it is not possible to deduce the temporal dynamics of the ionization process. When a photoelectron can be described by a wavefunction, or more precisely a wavepacket in the case of ionization by a light pulse, both its phase and amplitude need to be characterized in order to fully determine its properties and its time evolution. The energy variation of the photoelectron and its temporal evolution are inherently connected via Heisenberg's uncertainty principle,

$$\Delta\epsilon\Delta\tau \geq \frac{\hbar}{2} \tag{1.1}$$

where $\hbar$ is the reduced Planck's constant, $\Delta\tau$ can be understood as the temporal scale of the dynamics and $\Delta\epsilon$ as the energy needed to initiate it. For example, the ionization potential of helium is $\Delta\epsilon \approx 25$ eV, leads to a time of evolution on the scale of $\Delta\tau \geq 13$ as (10^{-18} s). This defines the natural timescale of electronic motion to be on the order of attoseconds.

To capture this ultrafast electronic motion, we need ultrashort, high-frequency light pulses. The development of short pulses has evolved rapidly since the invention of the laser in 1960 [4] thanks to *Q-switching* [5], with pulses in the nanosecond regime (10^{-9} s), *mode-locking* [6, 7], with pulses in the picosecond (10^{-12} s [8]) and femtosecond regime (10^{-15} s, [9]). This opened the door for the new field of *femtochemistry*, first introduced by Zewail [10], allowing for the study of chemical reactions on their natural timescale. The *Chirped Pulse Amplification* (CPA) technique invented by Strickland and Mourou (and later earning them a Nobel prize) [11], allowed the production of high-powered, ultrashort-pulsed lasers.

A key breakthrough was the discovery of High-order Harmonic Generation (HHG [12]), which enabled the generation of pulse trains in the Extreme UltraViolet (XUV) range, with durations on the order of hundreds of attoseconds. The duration of the attosecond pulses in a pulse train was first measured by Paul et al. [13] through a method known as *Reconstruction of Attosecond Beating By Interference of Two-photon transitions* (RABBIT). RABBIT is a photoelectron spectroscopic technique, where interferences between two-photon transitions involving high-order harmonics and the InfraRed (IR) probe field with a variable delay enables determination of the relative phase between consecutive harmonics. Other methods, such as Streaking [14], has also proven successful in determining the pulse duration of attosecond pulses. L'Huillier, Agostini and Krausz later earned a Nobel prize in 2023 for their contribution to attosecond science.

In general, the information obtained from a RABBIT or Streaking measurement reflects not only the properties of the attosecond pulses, but also those of the photoionization process. This has been used to study non-resonant photoionization of atoms [15–17], molecules [18, 19], and solids [20, 21]. Resonant processes introduce additional structure and complexity due to the involvement of intermediate or quasi-bound states. This thesis focuses more specifically on bound resonant ionization [22, 23], and auto-ionizing resonances [24–26], where strong coupling between discrete and continuum states leads to complex interference effects and temporal dynamics.

RABBIT and similar methods rely on wave formalism. As such, they assume that the photoelectron wave-packet retains full coherence and can be described by a wavefunction, with phase and amplitude. However, this is not always possible. Sometimes, due to experimental fluctuations or the contribution of multiple (incoherent) pro-

cesses, the photoelectron wave-packet might be subject to what is called *decoherence*. The influence of entanglement (for example between the ion and the electron) and decoherence in atomic and molecular photoionization [27, 28], has been previously investigated within the field of attosecond science [29–34]. Recently, a Quantum State Tomography (QST) protocol called Mixed-FROG, allowing the reconstruction of the density matrix of a photoelectron, created by the absorption of an Attosecond Pulse Train (APT) has been experimentally demonstrated [35].

1.2 Synopsis

Understanding the quantum nature of the photoionization process at the attosecond timescale imposes stringent requirements on experimental precision, stability, and flexibility. This thesis addresses these challenges by the implementation of a novel experimental setup that enables attosecond metrology with unprecedented stability, control, and spectral-resolution. This allows us to explore resonant photoionization in helium and argon using high-resolution RABBIT measurements, and extend attosecond science beyond wave-based methodology, using a new QST protocol for photoelectron wave-packets (KRAKEN, a Swedish acronym for *Kvanttillstånds tomogRafi av AttoseKund ElektroNvågpaket*). Together, these developments mark a step forward in probing and reconstructing ultrafast quantum processes.

1.3 Outline

This thesis is based on six papers, categorized into three themes: (i) experimental development, (ii) RABBIT-based investigations, and (iii) KRAKEN-based QST. A seventh paper is included in Appendix, but its content is not discussed in the main body of this thesis.

In **Paper I**, we present an ultra-stable and versatile Mach-Zehnder interferometer for high-energy resolution attosecond pump-probe photoelectron spectroscopy. By actively stabilizing the interferometer directly on the phase relation between the pump and probe, we are able to maintain low temporal jitter and independent control of the spectral profiles of the pump and probe. This allows for an easy switch between the two main protocols used, RABBIT and KRAKEN.

In **Paper II** and **III**, resonant photoionization using the RABBIT protocol is studied in argon and helium, respectively. In **Paper II**, we study the photoionization of argon atoms across the $3s3p^6 4p$ Fano resonance with high spectral-resolution RABBIT measurements. A variation of the measured spectral phase larger than π is found,

depending on the experimental conditions, due to the interaction between final states reached by two-photon transitions. In **Paper III**, resonant two-photon ionization via the 3p, 4p and 5p Rydberg states in helium is studied. With the help of angle-resolved, angle-integrated, and energy-resolved RABBIT measurements, we interpret the observed phase variations as functions of angle and energy using perturbation theory.

In **Paper IV-VI**, simulations and experiments using the KRAKEN protocol are presented. **Paper IV** provides a theoretical description of the protocol, supported by numerical simulations. Using a bichromatic probe with phase-locked spectral components, we can couple different spectral parts of the photoelectron wave-packet to the same final energy. Photoelectron spectra are recorded as a function of the pump-probe delay for different bichromatic frequency separations from which we determine the density matrix. In **Paper V**, the first KRAKEN measurements are presented. The density matrices of photoelectrons from helium and argon are measured and comparisons with theoretical calculations shows excellent agreement. Finally, in **Paper VI**, we demonstrate an improvement of the KRAKEN protocol, which uses a Golomb ruler for the probe spectrum. This enables the retrieval of multiple sub-diagonals in a single measurement, by simultaneously using the spectral and temporal domains more effectively.

The outline of the thesis is as follows: **Chapter 2** introduces the light sources used in all experiments, from the Ti:sapphire laser to the XUV APT, and the present interferometric experimental setup. **Chapter 3** describes resonant and non-resonant photoionization by the absorption of one and two photons. The RABBIT protocol and its experimental implementation are presented. Applications to resonant photoionization are briefly described. In **Chapter 4**, the QST protocol, KRAKEN, and its experimental implementation are presented. An improvement to reduce the experimental retrieval time, Poly-KRAKEN, is proposed. Finally, **Chapter 5** contains a short summary and an outlook.

Chapter 2

Experimental methods

In this chapter we briefly present the experimental methods used in this thesis. We describe the femtosecond laser system (Section 2.1), high-order harmonic generation in gases (Section 2.2) and the experimental setup, based on optical interferometry and photoelectron spectroscopy (Section 2.3 and **Paper I**).

2.1 The femtosecond laser system

2.1.1 Brief introduction to femtosecond light pulses

An optical pulse can be described by its complex amplitude

$$E(t) = \left|E(t)\right| e^{i\phi(t)+i\omega_0 t}, \tag{2.1}$$

where $\left|E(t)\right|$ is the amplitude of the complex temporal envelope, $\phi(t)$ is the temporal phase and ω_0 is the carrier frequency. The complex spectral amplitude, is the Fourier transform of $E(t)$,

$$\tilde{E}(\omega) = \frac{1}{\sqrt{2\pi}} \int_{-\infty}^{\infty} dt E(t) e^{-i\omega_0 t} = \left|\tilde{E}(\omega)\right| e^{i\varphi(\omega)}, \tag{2.2}$$

where $\left|\tilde{E}(\omega)\right|$ is the amplitude of the complex spectral envelope and $\varphi(\omega)$ is the spectral phase. An optical pulse is often described as a Gaussian pulse,

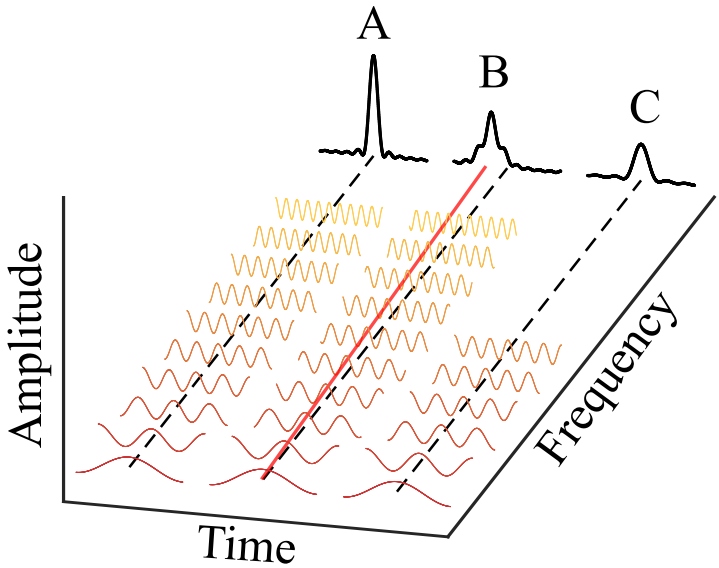

Figure 2.1: Oscillations with increasing frequencies (red to yellow). The summed intensity is shown in black. The black dotted line denotes the position of a reference time t_0. The red line indicates a linear shift of the position of the central maxima of the oscillation as a function of frequency. In A, ten spectral components are in phase, in B the same ten spectral components exhibit a quadratic phase and in C only the first five spectral components in phase are present, both leading to a longer pulse than in A.

$$E(t) = |E_0|\, e^{-4ln2\frac{t^2}{\Delta t^2}} e^{i\phi(t)+i\omega_0 t}, \tag{2.3}$$

where $|E_0|$ is the amplitude and Δt is the pulse duration, defined as the Full Width at Half Maximum (FWHM) of the intensity. The pulse duration and spectral bandwidth $\Delta\nu$, are related by the time-bandwidth product

$$\Delta t \Delta \nu \geq 0.44, \tag{2.4}$$

where $\nu = \omega/2\pi$. Ultrafast pulses require a broad spectral width. In Fig. 2.1, we can clearly see that the duration of the temporal pulse displayed in A is much shorter than that of the pulse in C, since the number of frequency components contributing to the total spectral intensity is higher. A broad spectrum does not however, necessarily lead to an ultrafast pulse. This can be understood by introducing the instantaneous angular frequency

$$\omega(t) = \omega_0 + \frac{\partial\phi(t)}{\partial t}. \tag{2.5}$$

If the temporal phase is either constant or has a linear dependency on time, the instantaneous frequency remains independent of time and all frequencies within the envelope of the pulse are synchronized. However, any quadratic temporal phase $\phi(t) \propto t^2$, leads to an instantaneous frequency with a linear dependence $\omega(t) = \omega_0 + bt$. This effect is known as *chirp*, where

$$b = \frac{\partial^2 \phi(t)}{\partial t^2}, \tag{2.6}$$

is the chirp parameter quantifying its magnitude. In this case the pulse duration becomes longer which can be seen by comparing A and B in Fig. 2.1. The number of frequency components are the same, however, in A, the phase is constant, while in B it is quadratic. The shortest pulse possible is obtained with a constant or linear temporal phase, which is known as Fourier Transform Limited (FTL), with $\Delta t \Delta \nu \approx 0.44$.

2.1.2 Ti:Sapphire oscillator

In our laboratory we use a *Laser Quantum venteon CEP5*, titanium (Ti^{3+}) doped sapphire (Al_2O_3) oscillator (Ti:Sa [36]), with an output spectrum covering >300 nm, centered at 800 nm, generating close to FTL pulses with a duration <6 fs, with 3 nJ of energy per pulse at 80 MHz repetition rate. The Ti:Sa is pumped with a continuous wave (CW) laser at 532 nm, allowing for both CW and pulsed lasing. To achieve short pulses one first has to sustain multiple longitudinal modes, such that the length of the entire resonator (from the end mirror (EM) to the outcoupler (OC)) is a multiple of half the mode's wavelength. Secondly, these modes must also be locked in phase with each other. As illustrated in Fig. 2.1 A, if the oscillator can sustain a large amount of these phase-locked modes, a short pulse may be created. Two additional conditions are required, a gain medium with a large gain bandwidth such as the Ti:Sa crystal, and a mechanism to favor mode-locking and consequently short-pulse lasing.

We achieve mode-locking through a passive technique known as Kerr Lens Mode-locking (KLM [7]) (See Fig. 2.2). In KLM, third-order nonlinear effects present in the gain medium, make the refractive index intensity-dependent, resulting in self-focusing within the gain medium. Since the instantaneous intensity is different for the CW and pulsed outputs, they will exhibit different spatial properties. The cavity layout in combination with the Kerr lens leads to a better overlap of the mode-locked pulses in the gain medium, and thus to a higher gain for the pulsed operation than for CW. However, to reach a more stable regime, the process must be initiated by an adjustable mirror (AM) that perturbs the laser into stable pulsed operation. The dispersion introduced by propagation through the crystal and air in the cavity is compen-

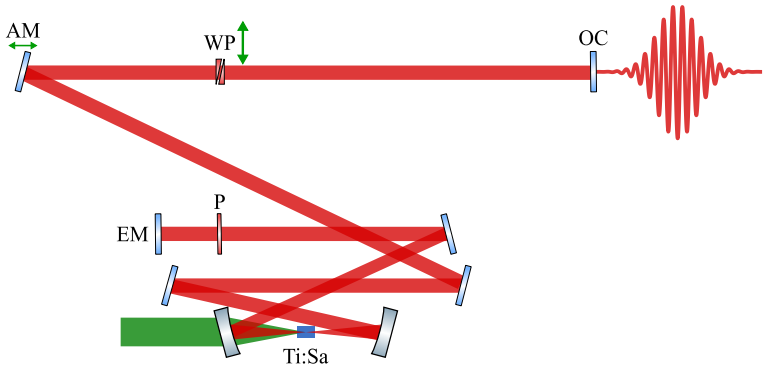

Figure 2.2: A schematic of the Ti:Sa oscillator used in the present work. The gain medium is Ti:Sa, and the oscillator cavity is extended between the end mirror (EM) and the output coupler (OC). A tunable BaF_2 wedge pair (WP) and thin BaF_2 plate (P) compensate for any dispersion and an adjustable mirror (AM) is used to obtain mode-locking.

sated for by dispersion compensating mirrors, an adjustable Barium Flouride (BaF_2) wedge pair (WP) and a glass plate (P). Amplification of the oscillator output is carried out at 1 or 3 kHz. Thanks to Ti:Sa's high thermal conductivity, these repetition rates can still support the generation of high-power ultrafast pulses, making the Ti:Sa laser a cornerstone of ultrafast science [37].

2.1.3 Chirped pulse amplification

Short pulses lead to high peak intensities that may induce unwanted nonlinear effects and/or damage to the gain medium it self. A solution to this is to broaden the pulse using dispersive elements such as a wedge pair or as in our case, a pair of gratings (see Fig. 2.3), before amplifying. The technique is known as *Chirped Pulse Amplification* (CPA [11]). The peak intensity of the chirped pulse is much lower, allowing amplification in the gain medium without any unwanted effects. The amplified and stretched pulse is then compressed by another grating pair, such that the total path length through the stretcher and compressor is equal for all spectral components. Thus high-power ultrashort pulses can be obtained.

2.1.4 Beamline

In Fig. 2.4, we show a schematic of the most important components in our laser system. The stretcher consists of a single grating and a retro reflector in an aberration free Öffner triplet configuration [38]. We then send the pulses into a *Fastlite Dazzler* [39], which is an Acousto-Optical Programmable Dispersive Filter (AOPDF), allowing for shaping of the spectral phase and amplitude. The bandwidth output after the DAZ-

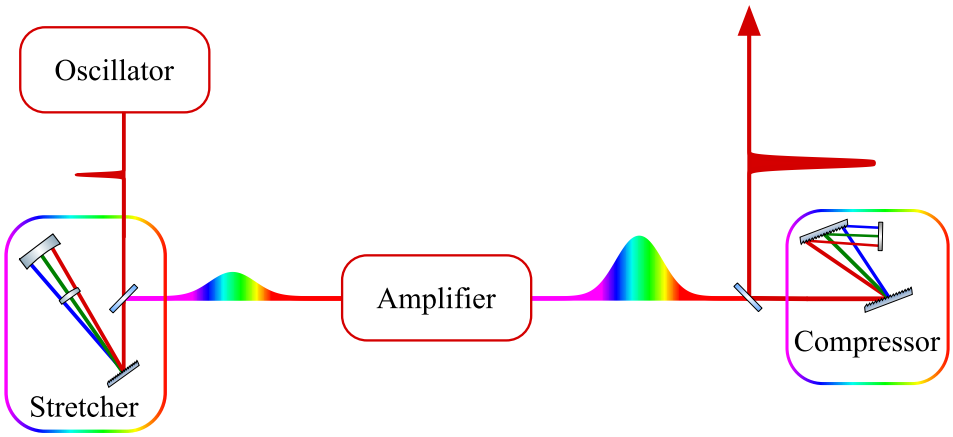

Figure 2.3: An illustration of Chirped Pulse Amplification (CPA): A short, low-energy pulse is first generated by an oscillator. This pulse is then stretched in time by a stretcher, reducing its peak power while maintaining its total energy. The stretched pulse is subsequently amplified, increasing its energy without damaging the amplification medium. Finally, the pulse is recompressed to a short duration, resulting in a high-energy, ultrashort pulse.

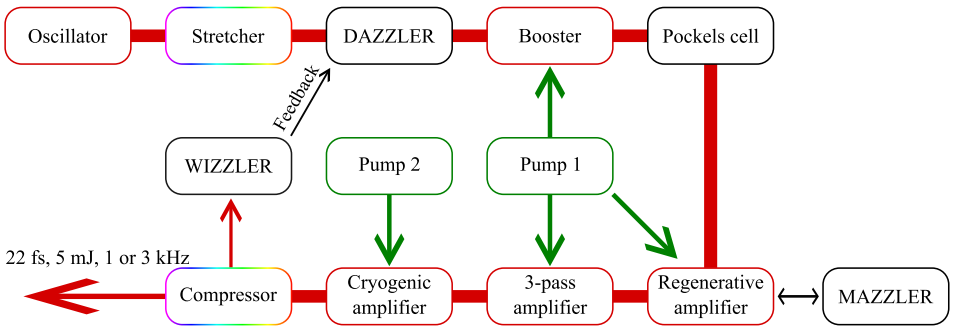

Figure 2.4: A schematic of the most important components and their interaction with each other, of the laser system used in this thesis.

ZLER is chosen to be almost 100 nm, but can be reduced[1]. The central wavelength of the pulse can be independently controlled between 780-830 nm. This has been used in **Paper II** and **III**, to ensure resonant ionization, covered in the next chapter.

The amplification is done in four stages of Ti:Sa crystals, pumped by two frequency doubled Neodynium-doped Yttrium-Lithium-Floride (Nd:YLF) *Continuum Terra lasers*, with a central wavelength of 527 nm. The first stage is a 7-pass booster amplifier, followed by a Pockels cell, selecting single pulses with a repetition rate of 1 or 3 kHz. In the second stage the pulses are amplified in 14 round trips (regenerative amplifier), followed by a second AOPDF (*Fastlite MAZZLER*), used to counteract gain narrowing [40]. To mitigate the spectral shape caused by the oscillator and amplification,

[1]Reducing the bandwidth increases the pulse duration to about 40-50 fs.

one selectively introduces loss in the high-intensity regions of the spectrum, allowing the MAZZLER to produce a flatter and broader output spectrum. The third stage is a 3-pass amplifier. The first three amplifiers all use pump 1 for amplification. The final stage is another 3-pass amplifier, cryogenically cooled to -190° to avoid thermal lensing and damage [41]. After the amplification stages, we achieve pulse energies from to 7.5 to 10 mJ.

The pulses are then compressed to near FTL pulses of ≥ 22 fs, using two holographic gratings in a Treacy configuration [42]. Due to the low efficiency of the compressor gratings (≈ 65 % after 4 passes), the final pulse energy is between 4.5 to 6.5 mJ. A weak reflection is sent to a *Fastlite WIZZLER*, providing a single shot measurement of the spectral phase and amplitude [43, 44]. The results are then sent to the DAZZLER, in a feedback loop such that one can optimize the spectral phase and compensate for dispersion caused the whole laser chain until the generation chamber.

2.2 High-order harmonic generation

The shortest possible pulse duration is fundamentally limited by the time-bandwidth product Eq. (2.4). However, there is a practical limit to how short a pulse can be generated for a given wavelength. This is known as the single-cycle limit, and it corresponds to approximately 2.67 fs for light with a central wavelength of 800 nm. To achieve sub-fs pulse durations, the central wavelength has to be well into the Extreme UltraViolet (XUV) regime. These frequencies can be reached by nonlinear processes. In the nonlinear regime, optical properties of the medium may be modified by a strong electric field, and in return, alter the driving field itself, leading to new frequencies. The first non-linear optical process observed, shortly after the invention of the laser in 1960 [4], was second harmonic generation in quartz, by Franken et al. in 1961 [45]. As the strength of the driving field increases, higher-order harmonics may be generated [12, 46].

High-order Harmonic Generation (HHG) was first observed in the late 80's [12, 46]. As illustrated in Fig. 2.5, the generated spectra can be schematically divided into three distinct regions. First, a perturbative region where the intensity of the harmonics decreases exponentially with harmonic order q. This region is followed by the appearance of a plateau, which cannot be explained within the framework of perturbative nonlinear optics. Finally, another sharp decrease occurs in the so called cut-off region. This phenomenon has been observed in noble gases [12, 46], molecules [47], solids [48] and liquids [49]. Due to the high intensity of the generating electric field, the atomic potential may be significantly distorted. Hence, the light-matter interaction requires a non-perturbative description.

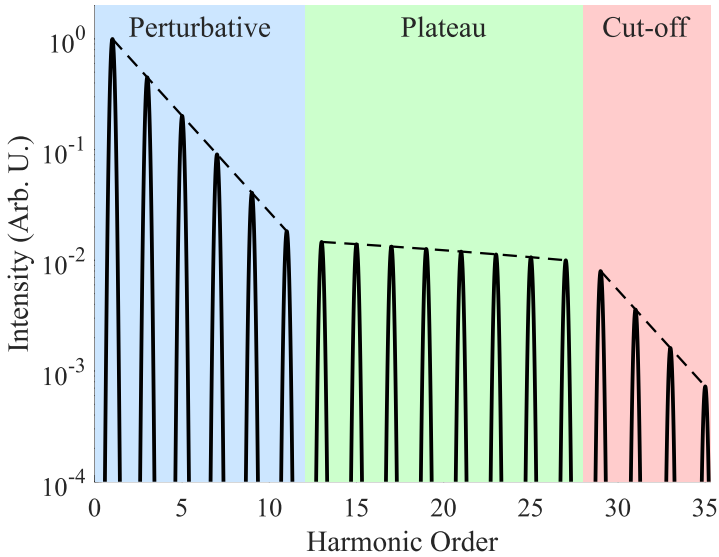

Figure 2.5: An illustration of the spectra generated through HHG. From the left, a quick decline in spectral intensity in the perturbative region (blue), followed by a plateau with almost constant spectral intensity (green). Another quick decline then follows in the cut-off region (red).

2.2.1 The three-step model

The Three-Step Model (TSM) was first introduced with a semi-classical approach [50, 51], later improved with a fully quantum mechanical model known as the strong field approximation [52]. In this thesis, we will only cover the semi-classical approach, since it can explain most spectral and temporal features of high-order harmonics. Fig. 2.6 shows the three steps of the model. In step (1), the atom is exposed to a strong electric field (red dotted line) that significantly distorts the atomic potential (black dotted line). The total potential (blue line) forms a barrier that is thinnest at the peak of the electric field, where the tunneling probability is the highest. The electron may then tunnel ionize through the barrier. In step (2), the electron is accelerated away from the parent ion by the electric field. As the electric field changes sign, the electron is driven back towards the parent ion, with a non-zero momentum. Finally, in step (3), the electron may recombine with the parent ion, leading to the emission of an XUV photon with energy given by $\hbar\Omega = I_p + \epsilon_k$, where Ω is the angular frequency of the generated photon, I_p the ionization potential and ϵ_k the kinetic energy of the electron gained in step (2).

The electron trajectories through the continuum in step (2) can be calculated by solving Newton's equations of motion for a charged particle, exposed to the Lorentz force. Assuming a driving electric field equal to $|E_0|\sin(\omega_0 t)$, linearly polarized in the x-direction, the electron acceleration in this direction is given by

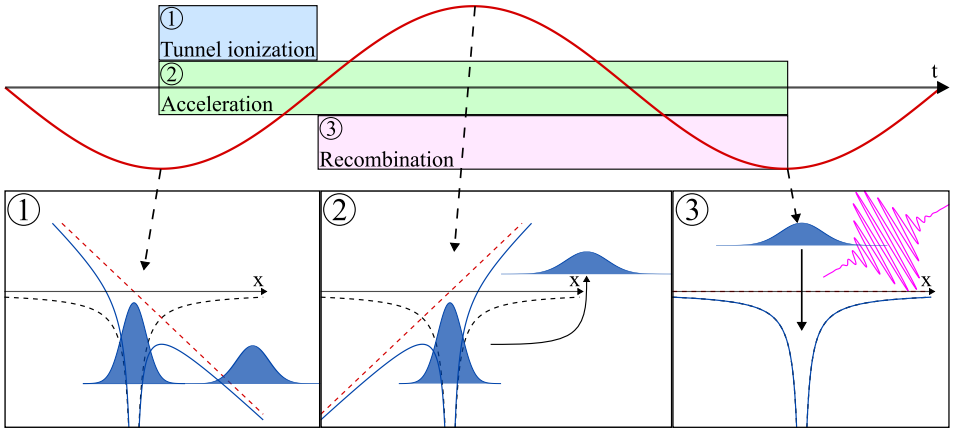

Figure 2.6: An illustration of the TSM. At the top, the three steps are shown relative to the electric field oscillation as a function of time. (1) Tunnel ionization that may lead to recombination (blue) starts at the peak of the field and stops when the field changes sign. (2) From the time the electron is ionized until it recombines it is exposed to the oscillating electric field (green). (3) The electron may recombine from the time the electric field first changes sign, until a full laser cycle after the start of step (1). At the bottom, a segment of each of these processes is illustrated.

$$m_e \frac{\partial^2 x(t_i,t)}{\partial t^2} = -e|E_0|\sin(\omega_0 t), \tag{2.7}$$

where m_e is the electron rest mass, e the elementary charge and t_i is the time of ionization. The electron trajectory, assuming that the electron appears in the continuum at time t_i and position $x(t_i) = 0$, with zero velocity, is then given by

$$x(t_i,t) = \frac{e|E_0|}{m_e\omega_0^2}\left[\sin(\omega_0 t) - \sin(\omega_0 t_i) - \omega_0(t-t_i)\cos(\omega_0 t_i)\right]. \tag{2.8}$$

As shown in Fig. 2.7, electrons that are ionized before the peak of the driving field will never return to the parent ion ($x = 0$) (gray dashed lines). However, if ionization occurs between the peak and the sign change of the field, the electrons may return within a single cycle[2]. Because tunnel ionization can occur twice per electric field cycle, XUV radiation is emitted every half-cycle (see Fig. 2.7). Due to half-cycle periodic generation and interference in an isotropic medium, the resulting XUV radiation consists only of odd-order harmonics, spaced by $2\omega_0$. The kinetic energy of the electron when it returns is illustrated in color for the different trajectories, and is given by

[2]It is possible for electrons to return after a full cycle, however, the probability decreases rapidly with each additional pass [53].

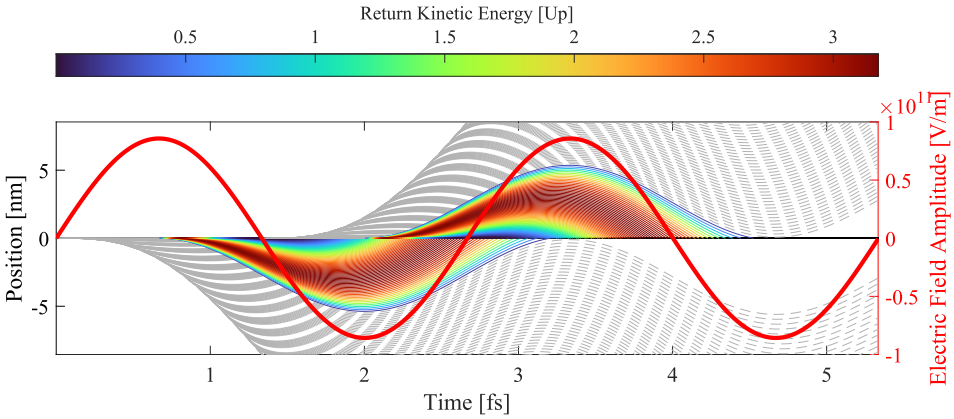

Figure 2.7: Classical electron trajectories around the parent ion are governed by Newton's equations of motion in the presence of an electric field. The electric field (red) accelerates electrons away from the parent ion until it changes sign, after which the electrons are accelerated back toward the ion. If electrons tunnel ionize before the peak of the electric field, they undergo strong acceleration away from the ion and may never return (gray dashed lines). The trajectories are shown in color according to the kinetic energy they return with, expressed in terms of the ponderomotive energy. Electrons may tunnel ionize twice per laser cycle, as the field exhibits two peaks of opposite sign.

$$\epsilon_k(t_i, t_r) = 2U_p \left[\cos(\omega_0 t_r) - \cos(\omega_0 t_i)\right]^2, \tag{2.9}$$

where t_r is the return time of the electron and U_p is known as the *ponderomotive energy*, given by

$$U_p = \frac{e^2 E_0^2}{4 m_e \omega_0^2} \propto \lambda_0^2 I, \tag{2.10}$$

where λ_0 is the wavelength of the driving field and I the peak intensity given by $I = c\epsilon_0 |E_0|^2 /2$, where c is the speed of light and ϵ_0 the vacuum permittivity. The TSM successfully predicts both the start and end of the plateau. The plateau begins with the first odd harmonic whose energy exceeds the ionization potential I_p of the medium. The cut-off corresponds to the maximum photon energy, obtained when the electron recombines with its parent ion after gaining $3.17U_p$, (see Fig. 2.7 and 2.8) and is given by

$$E_{\text{cut-off}} \approx I_p + 3.17U_p. \tag{2.11}$$

It is possible to extend the plateau by increasing the wavelength of the driving field. However, the HHG conversion efficiency scales poorly with increasing wavelength ($\approx \lambda^{-5} - \lambda^{-9}$ [54]). One could also increase the intensity and thereby the acceleration

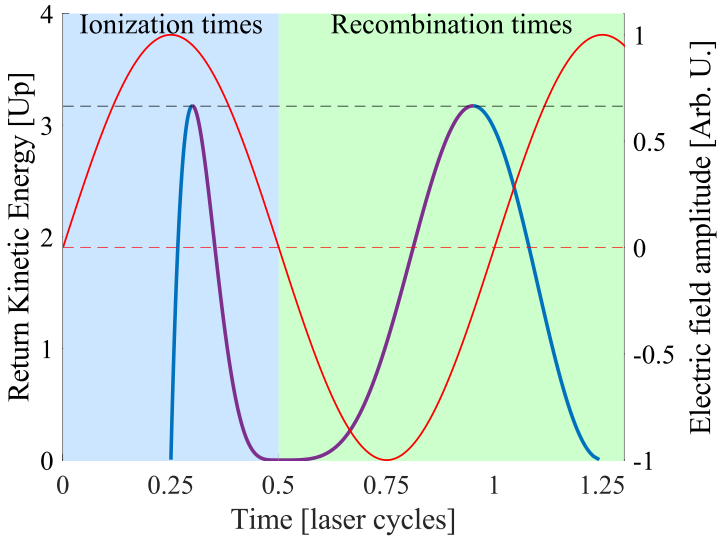

Figure 2.8: Kinetic energy of the returning electron as a function of ionization (blue background) and return times (green background). The electric field (red) accelerate the electrons such that the maximum kinetic energy is $3.17U_p$. All other return kinetic energies can be obtained by either the short (purple) or long (blue) trajectories.

experienced during the electron trajectories in Step 2. This is however limited by the depletion of the single-atom ground state and the macroscopic phase-matching conditions (see Subsection 2.2.2).

As can be seen from Fig. 2.7 and 2.8, apart from the maximum kinetic energy, all kinetic energies may be obtained for two sets of ionization and return times. The two families of trajectories are called short and long, depending on whether the electron recombination time is shorter or longer than the trajectory leading to the cut-off energy. They are indicated in purple and blue in Fig. 2.8, respectively.

2.2.2 Phase-matching

Atom emissions throughout the gas medium must be phase-matched in order to achieve any significant conversion efficiency of the HHG process, as illustrated in Fig. 2.9. In A, the individual contributions from single atoms have random phase relation, while in B they are phase-locked, generating a field with a significantly higher amplitude. The condition required for phase-matching can be expressed using the wave vectors of the fundamental (k_0) and of the harmonic fields (k_q) as

$$\Delta k(q) = qk_0 - k_q = 0. \tag{2.12}$$

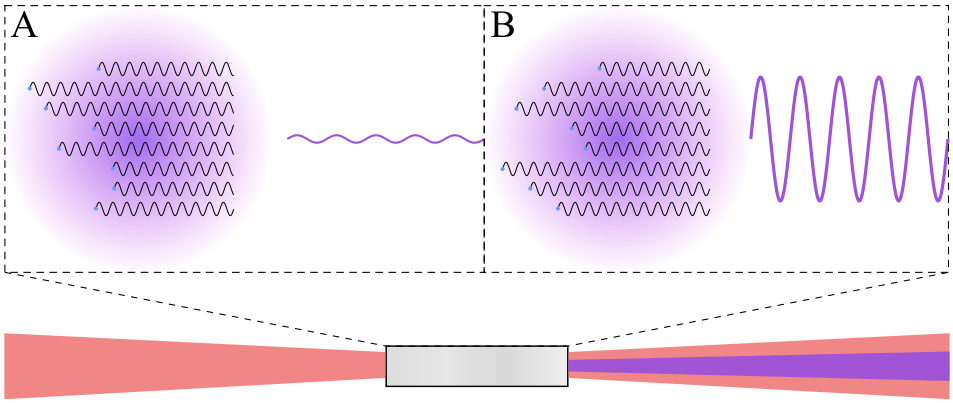

Figure 2.9: Illustration of incoherent (A) and phase-locked (B) harmonic emission. Coherent buildup leads to significantly enhanced XUV output.

The total wave vector mismatch can be decomposed into four contributions [55],

$$\Delta k = \Delta k_n + \Delta k_p + \Delta k_g + \Delta k_d, \tag{2.13}$$

where Δk_n arises from the neutral gas dispersion, Δk_p from the electron plasma dispersion, Δk_g originates from the geometrical phase (Gouy phase) due to the focusing of the driving field and Δk_d is the phase acquired during the electron trajectory in step 2 of the TSM. Δk_n is proportional to the gas density and is always positive, while Δk_p, which rapidly varies with the intensity of the driving field, is always negative. The neutral atom and electron plasma dispersion varies linearly with the gas pressure. While the XUV flux may initially increase with gas pressure, eventually either the plasma density or the probability for reabsorption of the XUV light will become too high, and the conversion efficiency will drop significantly [56]. The free electron density also results in a blue-shift of the fundamental frequency [57].

The contribution of the Gouy phase (Δk_g) depends on the focusing of the driving field and the position of the medium relative to the laser focus. It is always negative. Lastly, the contribution of the electron trajectory (Δk_d) depends on the intensity. Since the electron spends a different amount of time in the continuum for the short and long trajectories, phase matching may select only one of them. Δk_d changes sign across the focus, such that for $z < 0$, Δk_d is negative, and for $z > 0$, positive. In our experiments we align the gas cell so that $z > 0$ (after the focal plane), so that $\Delta k_n + \Delta k_d = \left|\Delta k_p\right| + \left|\Delta k_g\right|$.

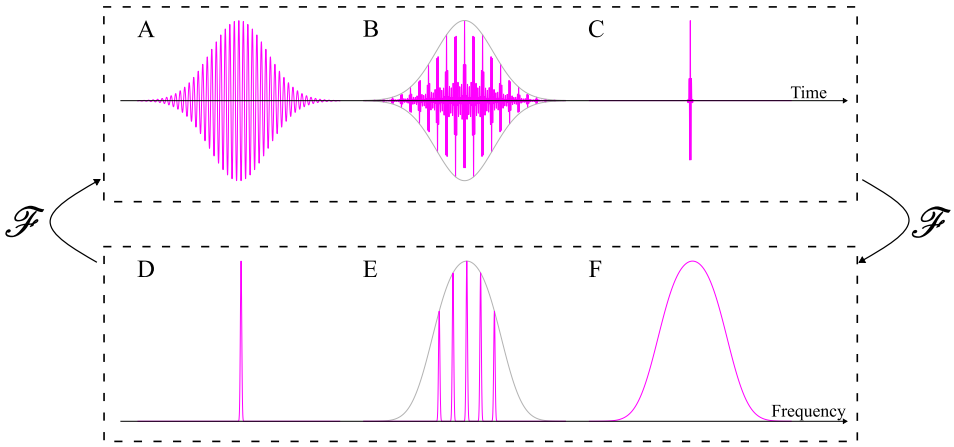

Figure 2.10: An illustrates the time-frequency relationship between pulses and their frequency representation. A femtosecond XUV pulse envelope (A), corresponds to a single harmonic spectral peak (D). A phase-locked APT (B), corresponds to a frequency comb of harmonics (E). A single isolated attosecond pulse (C), corresponds to a broad envelope consisting of a continuum of frequencies (F).

2.2.3 Attosecond pulse train

Fig. 2.10 illustrates the time-frequency relationship between pulses and their frequency representation, where spectral components are assumed to be phase-locked (i.e. with the same phase). Fig. 2.10 D shows the spectral intensity of a single harmonic peak. By applying a Fourier transform to the harmonic spectral amplitude, as previously discussed in Section 2.1.1, we obtain the electric field of a femtosecond-duration harmonic (A), related to the duration of the driving field.

In contrast, a single isolated attosecond pulse (C) exhibits a broad spectral amplitude composed of a continuum of frequencies (F), representing its spectral envelope.

Through the HHG process, attosecond pulses with broadband continuum spectrum are generated every half cycle from a single atom. These interfere with each other, and result in a frequency comb of narrowband odd harmonics (see Fig. 2.10 E). In the time domain, this results in an APT, consisting of a sequence of attosecond pulses within a 'long' femtosecond envelope (B). Isolated attosecond pulses can be produced, by ensuring that only one half-cycle has sufficient intensity to generate harmonics in the cutoff [58].

In practice, the temporal structure of the harmonics is influenced by both *femtochirp* and *attochirp* [59–61], as well as the presence of multiple electron trajectories, which affect phase-locking and thus the formation of the APT. Selecting a single trajectory enables the generation of a clean APT.

2.3 Experimental setup

The setup, described in **Paper I**, implemented and used for all papers in this thesis is the focus of this section. The update to the experimental setup presented here was implemented at the beginning of this thesis and is an important part of my thesis work. Only the angular-resolved results in **Paper III** were obtained with the prior experimental setup, detailed in [62]. In order to perform attosecond interferometric measurements and the experiments described in Chapters 3 and 4, the relative path length between the pump and probe must be controlled with a very high precision. The fundamental frequency of the laser described in Section 2.1 is centered around 800 nm, so that the 2ω oscillation period sought in the RABBIT protocol (see Chapter 3) is $T/2$ = 1.33 fs. A realistic time step during a delay scan is a tenth of this, i.e. 133 as, which corresponds to a motion of the delay stage (about half as big as the beam path) equal to $cT/40 \approx 80$ nm. This precision has to be maintained for the entire duration of the experiment, sometimes several hours long. For the KRAKEN protocol described in Chapter 4, the delay must be scanned over a long range, since we need to be able to resolve two nearby peaks in the frequency domain. To be able to resolve a signal generated from two peaks separated by roughly 6 nm, we need at least a delay range of $\Delta T > \lambda^2/(c\Delta\lambda) \approx 400$ fs. A spectral-resolution much lower than, for example the Spin-Orbit (SO) splittings in argon (177 meV) as described in Chapter 3, is also required for the measurements attempted. Henceforth, we require a stable experimental setup, with high spectral-resolution and the possibility to have both small time steps and a long scan range.

Other requirements for this setup are the individual spectral control of the two interferometer arms, and in general an increased flexibility for novel experiments. The experimental setup implemented in this thesis is shown in Fig. 2.11. It is possible to choose between two beam paths for the pump beam (red) and the probe beam (yellow). For the highlighted beam path, we have the probe arm with the 4f-shaper coupled in, and the pump arm with the 4f-extension to keep both arms equally long. This configuration is used in **Papers IV-VI**. In reduced color, these extensions are not coupled in (**Paper II-III**).

2.3.1 Mach-Zehnder interferometer

The IR laser detailed in Section 2.1 is sent into a Mach-Zehnder interferometer with a 60/40 beam splitter (BS). Both the pump and probe arms include a delay stage. The pump pulse (red) goes through a femtosecond scale delay stage (FS) for both coarse delay adjustments and/or long delay scans, while the probe pulse (yellow) is reflected by an attosecond scale piezo stage (AS) for fine adjustments. In both arms,

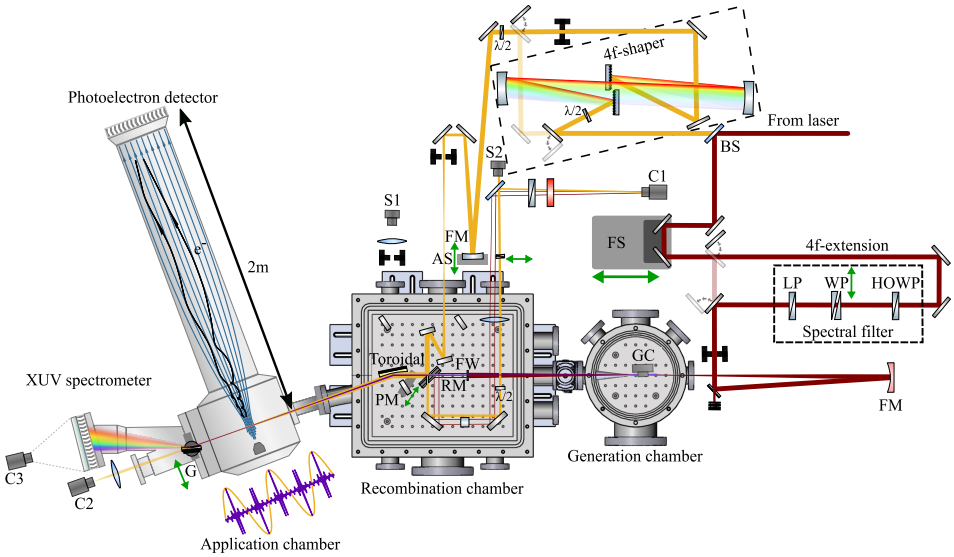

Figure 2.11: An illustration of the new attosecond interferometer, detailed in **Paper I**. The paths of the pump, probe and XUV are shown in red, yellow and purple respectively. The setup can be divided into eight main parts: a Mach-Zehnder interferometer (from BS to RM), a 4f-shaper, a spectral filter, a generation chamber, a recombination chamber, a photoelectron detector, an XUV spectrometer and an active temporal stability scheme (from RM to C1). The following components are: BS, beam splitter; FS, femtosecond scale delay stage; HOWP, high-order waveplate; WP, wedge pair, LP, linear polarizer; FM, focusing mirror; GC, gas cell; FW, filter wheel; RM, recombination mirror, $\lambda/2$, half-waveplate; AS, attosecond scale piezo stage; PM, pick-up mirror; G, concave grating; C_i, Camera i; S_i, spectrometer i. Adapted from **Paper I**.

two flip mirrors allow us to couple the 4f-shaper/extension in or out depending on the configuration needed. In the 4f-extension of the pump arm, similar to a single stage Lyot filter, a spectral filter consisting of a high-order-quartz waveplate (HOWP) at a 45° angle relative to the incoming polarization, a birefringent wedge pair (WP) and a linear polarizer (LP) are introduced. The HOWP applies wavelength-dependent phase retardation to the pump pulse. The WP allows us to tune the total order applied so that the relative phase between the two polarization arms may vary between 5-15 full rotations (each rotation corresponds to a phase retardation of 2π). The transmitted spectrum after the LP is modulated by a tunable sinusoidal function, which gives us control over the central wavelength, the spectral width, and the outgoing polarization of the pump field.

Both the pump and the probe are focused with focusing mirrors (FM), with the same focal length of f=50 cm, so that their spatial properties remain similar. The central part of the pump is blocked before being focused, to limit the stress on the metallic filters on the filter wheel (FW). These are only about 200 nm thick, and are hence quite sensitive. The outer part of the pump is focused into the gas cell in the generation chamber to drive the HHG process as detailed in Section 2.2. The resulting XUV

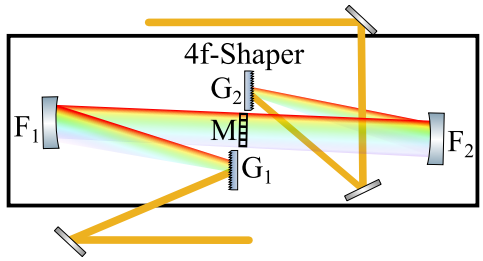

Figure 2.12: An illustration of the 4f-shaper with two reflective diffraction gratings (G_i), two focusing mirrors (F_i) and a mask (M). The separation between the different elements is the same as the focal length of the focusing mirrors, hence the name: 4f-shaper.

and pump IR goes through the filter wheel (FW), see Fig. 2.14. Only the the outer pump IR passes through the fused silica plate, while the central part of the pump IR is blocked by the aluminum foil [3]. For the XUV only the central part of the beam passes through the aluminum foil, while any outer part is blocked by the fused silica plate. The XUV and IR pump components are therefore spatially separated after the filter wheel, which is explained further in Section 2.3.3. The pump and probe are finally recombined, completing the Mach-Zehnder interferometer, at the recombination mirror (RM), detailed in 2.3.2 and 2.3.3.

2.3.1.1 4f-shaper

The probe path includes another type of spectral filter, known as a 4f-shaper. As shown in Fig. 2.12, our 4f-shaper consists of two *Spectragon* 1200 lines/mm reflective diffraction gratings (G_i), two spherical mirrors (F_i), with a focal length of f = 50 cm, and a mask (M). The total length between the two gratings is 4f, which explains the name. The first grating and focusing mirror allow us to spatially separate the spectral components of the probe in the Fourier plane, where the mask is placed. By changing the position and shape of the mask in the Fourier plane, we have full control of the spectral shape of the probe, as shown in Fig. 2.13. Allowing us to perform experiments with specific requirements of the probe spectra, see **Paper IV-VI**. We measure the spectral phase before and after the 4f-shaper with a dispersion scan (d-scan, see **Paper VII** [63, 64]), to ensure the quality of the 4f-shaper (see **Paper I**).

The masks used in **Paper V** and **VI**, are shown in Fig. 2.13 A and B, respectively. In **Paper V**, we used a probe pulse with two spectral peaks. One is kept constant between measurements, while the other is tuned across the probe's bandwidth. The

[3]The type of metallic foil can be changed, for **Paper I-III** a single layer of aluminum was used, for paper **Paper IV-VI** a layer of germanium of varying thickness was added. Since we use an annular cropped beam, the central part is not so strong and does not damage the filters.

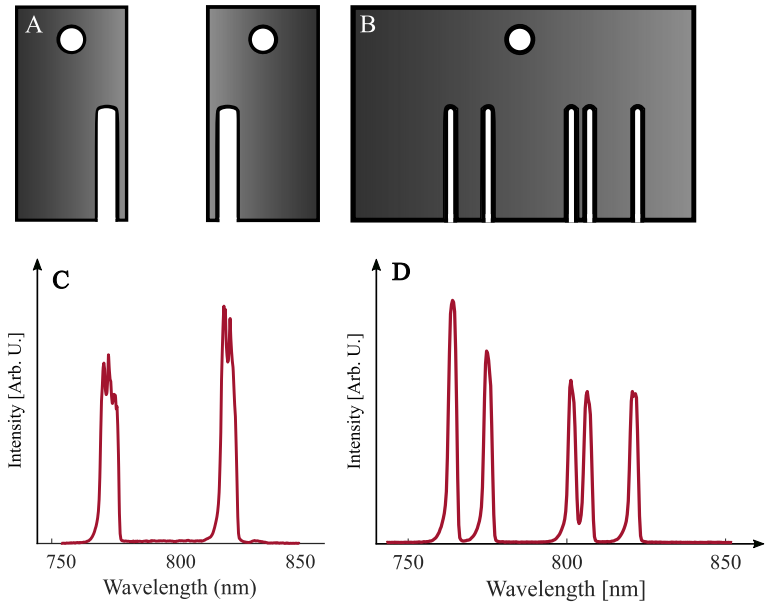

Figure 2.13: An illustration of the masks used for the KRAKEN (A) and Poly-KRAKEN (B) protocol. Experimentally measured spectra for respective protocols are shown in (C) and (D).

spectral profile shown in C is an example of a bichromatic probe used in one of these measurements. In **Paper VI**, a single mask is used leading to a probe field with five spectral components, shown in D. More information is given in Sections 4.1 and 4.3.

2.3.2 Application chamber

As is shown in Fig. 2.14, the pump XUV and the outer probe IR propagate to the gold-plated toroidal mirror (f=30 cm), to be refocused into a diffuse gas jet in a 2f-2f scheme, in the application chamber. The XUV and IR fields are then reflected on a concave grating (G) towards an XUV spectrometer. The grating can be moved out of the beam path, allowing the study of the IR pump and probe focus and spatial overlap with the help of a lens and camera C2. The spatial overlap in the application chamber can be improved by fine-tuning the RM using piezoelectric adjusters. The XUV spectrometer detector consists of a Micro-Channel Plate (MCP [65]), followed by a phosphor screen, and finally a camera (C3).

2.3.3 Active temporal stabilization of the Mach-Zehnder interferometer

Our setup requires careful and stable overlap of the pump and probe fields in both time and space. A pick-up mirror (PM) can be introduced between the RM and toroidal, to study the spatial or the temporal overlap. The temporal overlap is adjusted by looking at the spectral interferences on the spectrometer S1 [4].

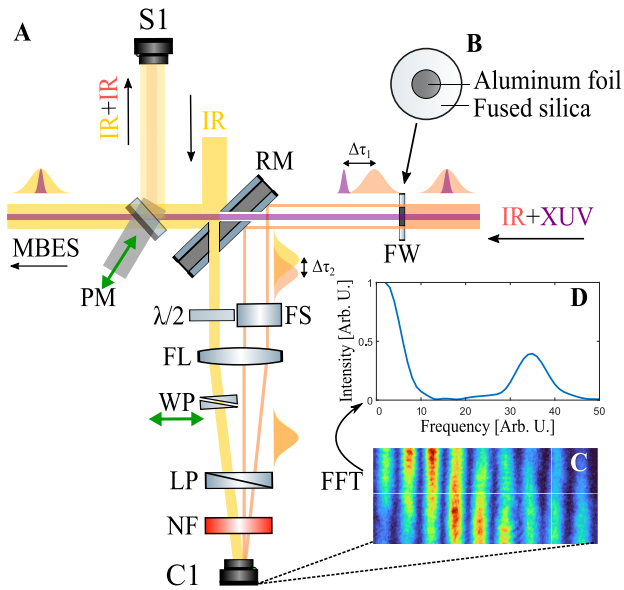

Figure 2.14: A schematic representation of the active temporal stabilization of the Mach-Zehnder interferometer. A the recombination of the pump and probe at the recombination mirror (RM), with the pump and probe IR in red and yellow respectively, while the XUV is shown in purple. The following components are: FW, filter wheel; PM, pick-up mirror; MBES, magnetic bottle electron spectrometer; S1, spectrometer 1; $\lambda/2$, half-waveplate; UVFS, UV fused silica block; FL, focusing lens; WP, wedge pair; LP, linear polarizer; NF, narrowband filter; C1, camera 1. In B, a sketch of the metallic filter mounted on a holey fused silica plate. In C, the spatial fringes recorded in C1 and in D, their FFT. For clarity, the mirrors folding the beam path out of the vacuum chamber (see Fig. 2.11) are removed from this figure. Adapted from **Paper I**.

The outer part of the pump IR and the central part of the probe IR are used for active temporal stabilization. The overlap of the two pulses does not coincide exactly with the temporal overlap of the XUV and the probe propagating towards the application chamber. As shown in Fig. 2.14, the pump XUV and IR are temporally separated ($\Delta\tau_1$) due to the difference in optical path lengths of the thin aluminum filters (a couple of hundreds of nm thick) and the fused silica plate (around 1.5 mm thick). An additional path length difference, due to the probe path travel through the RM ($\Delta\tau_2$), must also be taken into account. To compensate for this, a thick fused silica block (FS) is introduced into the pump arm, and a thin wedge pair (WP) into the probe

[4] To study the temporal overlap with the PM, we must not have any filter so the central part of the pump IR passes through the recomb chamber as well.

such that the actual temporal profile after the RM on the S_1 and the reference taken out on the camera overlaps [5]. The two beams are focused down with a focusing lens (FL), to spatially overlap on the camera, such that spatial fringes may be observed, as shown in Fig. 2.14 C. To improve the contrast of these fringes a half-waveplate ($\lambda/2$) in the probe and a linear polarizer (LP)[6], allowing us to vary the ratio of the two beams by adjusting the overlap on the camera. Finally, a narrowband filter can be added to extend the range within which the temporal overlap between the two arms can be detected. The fast Fourier transform (FFT) of the spatial fringes is extracted, as shown in Fig. 2.14 D, from which the spatial frequency and phase can be extracted. A PID-controller, controlling one of the delay stages, uses this signal as a feedback, where the phase is proportional to the pump-probe delay. This is how the delay is controlled and the interferometer is actively stabilized down to around 13 as Root-Mean-square (RMS) error over several hours (see **Paper I**). The stabilization is based directly on the phase relation between the pump and probe fields, as opposed to using a co-propagating CW HeNe laser [66], allowing for improved versatility.

2.3.4 Photoelectron Detectors

As previously mentioned, both the XUV pulse train and probe IR pulse are focused down into the application chamber, where a target gas is injected. Ionization of a gas by a combination of XUV and IR pulses, allows for experimental schemes such as RABBIT (see Section 3.2), and KRAKEN see Chapter 4. Both of these experimental schemes rely on detecting the photoelectrons as a function of delay between the XUV pump and IR probe fields. In all papers, a Magnetic Bottle Electron Spectrometer (MBES) is used, a schematic of which is presented in Fig. 2.15. In **Paper III**, a Velocity Map Imaging Spectrometer (VMIS) [67] is also used. This spectrometer allows for angular resolution and will only be briefly covered in this thesis.

Photoionization occurs in the overlap between the XUV/IR foci and the continuous effusive gas jet in the application chamber. The ionization rate is kept low such that a few events occur per pulse. The photoelectrons are then guided into a flight tube by a conically shaped NdFeB magnet placed on the opposite side of the chamber, close to the gas jet, delivering a strong, inhomogeneous magnetic field (100-1000 mT). The magnetic field has a 4π sr collection efficiency, parallelizing the electron trajectories towards the flight tube. Here, a weak, homogeneous magnetic field (0.1-10 mT) keeps the photoelectrons in stable trajectories along the 2 m long flight tube. The combination of these two magnetic fields forces the photoelectrons into helical trajectories

[5] Technically, only the two IR components will overlap fully due to this, meaning $\Delta\tau_1$ is unaccounted for. However, this is usually on the scale of hundreds of attosecond and is in practice compensated by a quick delay scan to find the true $\tau = 0$ before all experiments.

[6] It is a Wollaston prism, where the angle of refraction is different for different polarized components.

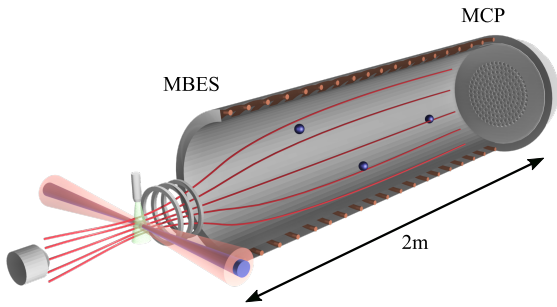

Figure 2.15: An illustration of the magnetic bottle electron spectrometer (MBES), used for all papers. Adapted from **Paper III**.

around the magnetic field lines, running parallel to the flight tube. At the end of the flight tube, a MCP amplifies the electron signal through a cascade of collisions. The entire flight tube is encased in mu-metal, shielding the electrons from any disturbances caused by the earth magnetic field.

The MBES is a Time-of-Flight (ToF) spectrometer. The generated photoelectrons follow classical trajectories in the flight tube, with a time of flight t_{ToF} related to the kinetic energy by

$$E_k = \frac{m_e}{2}\left(\frac{L+\gamma}{t_{\mathrm{ToF}}}\right)^2, \tag{2.14}$$

where m_e is the electron mass, L is the length of the flight tube and γ is a calibration parameter. t_{ToF} is measured with the help of a photodiode at the laser output that starts the recording time, which is stopped by the acquisition card when the detector signal is retrieved [7]. The sampling rate of the data acquisition card hence sets a lower limit to the energy resolution of the MBES, which can be expressed as $\delta E_k \propto L^2 t_{\mathrm{TOF}}^{-3}\delta t$. Since t_{TOF} increase linearly with L, it is clear that a longer flight tube improves the resolution of the spectrometer. The resolution of the MBES also depends on the kinetic energy, and the resolution of the MBES can also be expressed as $\delta E_k/E_k \propto \delta t/t_{\mathrm{TOF}}$. Our MBES, detailed in **Paper I**, has a measured resolution of $\delta E_k/E_k \approx 2\%$ at 1-2 eV. A tunable retarding potential may be applied along the flight tube, to slow down fast electrons for a better resolution. The MBES has a spectral-resolution below 80 meV, for kinetic energies below 5 eV.

Another limitation is that photoelectrons generated with the same kinetic energy, but ejected in two opposite directions may end up with two different t_{ToF}. For example,

[7] Any electronic signal delays also need to be accounted for.

one of these photoelectrons may be ejected directly towards the flight tube, while the other towards the strong magnet, to eventually be repelled towards the flight tube by the strong magnetic field. The extra time it takes for the second electron to enter the flight tube, appears as a 'tail' towards lower kinetic energies. This spread of the photoelectron kinetic energy can be understood through the convolution between the MBES Point-Spread Function (PSF) and the kinetic energy spectrum (S_{raw}) of the electron,

$$S_{measured}(\epsilon) = \int d\epsilon' \mathrm{PSF}(\epsilon') S_{raw}(\epsilon - \epsilon'). \tag{2.15}$$

The effects of the PSF can be removed by spectral deconvolution, if the spectral-resolution of the MBES as a function of kinetic energy is well characterized. In **Paper V-VI** spectral deconvolution algorithms based on blind Lucy-Richardson deconvolution are used to further increase the spectral-resolution [33, 68, 69].

In **Paper III**, both MBES and VMIS measurements were performed. While the MBES offers a 4π sr collection efficiency, it necessarily integrates over all emission angles, resulting in loss of angular information. A VMIS, on the other hand, allows angular channels to be resolved, enabling full characterization of the photoelectron emission. In the VMIS, photoelectrons produced are accelerated by electrostatic lenses and projected onto a MCP and phosphor screen, which is then imaged by a CCD camera, projecting the 3D momentum distribution onto a 2D plane. Assuming cylindrical symmetry, the angular distribution can be reconstructed using an inverse Abel transform. In **Paper III**, this was done using the pBASEX algorithm [70]. The energy resolution at low energies ($\delta E_k/E_k \approx 5\%$) is however lower than that of the MBES.

Chapter 3

Attosecond interferometry

In Section 3.1, the single and two-photon ionization processes that are studied in this thesis are formally described. The two-photon attosecond interferometric protocol known as RABBIT, fundamental to **Paper I-III**, is introduced in Section 3.2. Lastly in Section 3.3, the main results of **Paper II** and **III** are briefly described.

3.1 Ionization processes

3.1.1 Photoionization

Photoionization occurs when an atom absorbs a single photon with more energy than the atomic potential ($\hbar\Omega > I_p$). An electron is removed from the atom into the continuum, where it is no longer bound. The ionization of an atom from the ground state $|g\rangle$ by the absorption of a single XUV pulse with a bandwidth of $\delta\Omega$, populates a broadband superposition of continuum states $|\Psi\rangle_e$ (see Fig. 3.1).

Conventional photoelectron spectroscopy allows only measurement of the amplitude of the spectrum $S(\epsilon)$ [71] [1]. However, with the advent of attosecond photoelectron techniques, both the spectral amplitude and phase of the photoelectron wave-packet can be measured. This also enables the study of ionization dynamics in the time domain. Attosecond photoelectron interferometry, which is used in this thesis, utilizes two-photon transitions and is covered in the following sections.

[1] Angular resolved spectroscopy does allow for the retrieval of the relative phase between different angular parts of the spectrum.

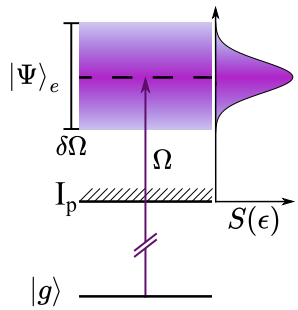

Figure 3.1: The energy diagram for single-photon ionization of an atom from its ground state $|g\rangle$, to a broad-band, continuous photoelectron state $|\Psi\rangle_e$. The central energy of the resulting photoelectron spectrum $S(\epsilon)$ is determined according to the XUV frequency Ω and the ionization potential of the atom, I_p.

3.1.2 Two-photon ionization

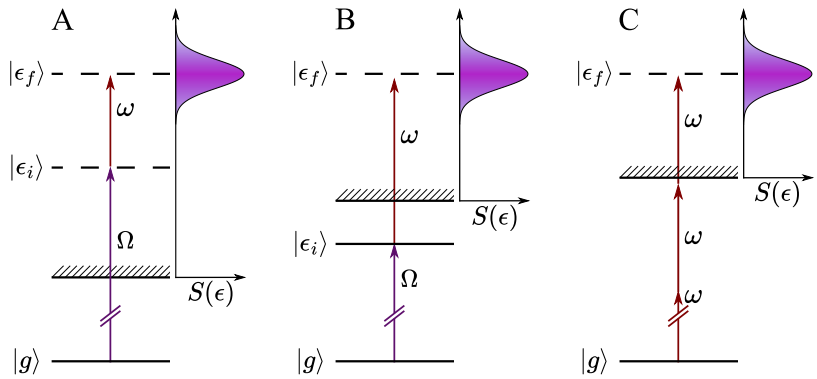

Figure 3.2: The energy diagram for a two-photon ionization of an atom from its ground state $|g\rangle$. In A(B), the atom is ionized(excited) by the absorption of a XUV photon to an intermediate continuous (bound) state, followed by the absorption of an IR photon (ionizing the atom) to the final continuous photoelectron state. A high IR intensity may result in multi photon ionization as represented in C.

As illustrated in Fig. 3.2 A (B), the atom is ionized (excited) by the absorption of an XUV photon to an intermediate continuous (bound) state $|\epsilon_i\rangle$, followed by the absorption of an IR photon (ionizing the atom) to the final continuous photoelectron state $|\epsilon_f\rangle$ [2]. The photoelectron wave-packet is centered around the final energy such that $\epsilon_f = \hbar(\Omega + \omega) + \epsilon_g$, where $\epsilon_g = -I_p$ for a neutral atom in its ground state [1]. Assuming that both the XUV and IR fields are linearly polarized along $\hat{z}$, the two-photon transition matrix element between the initial state $|g\rangle$, and the final state $|\epsilon_f\rangle$ can be calculated based on second-order perturbation theory as [15]

[2]The IR can be absorbed before the XUV, but this much less probable [72]

$$M_{g,\epsilon_f}^{(\pm)}(\Omega) \propto \lim_{\epsilon \to 0^+} \sum\!\!\!\!\!\!\int_i \frac{\langle \epsilon_f | \hat{z} | \epsilon_i \rangle \langle \epsilon_i | \hat{z} | g \rangle}{\hbar\Omega + \epsilon_g - \epsilon_i + i\epsilon}, \tag{3.1}$$

where the integral sum runs over all continuum and discrete intermediate states $|\epsilon_i\rangle$. The two-photon matrix element becomes significantly large when $\epsilon_i = \hbar\Omega + \epsilon_g$, which is the case for resonant two-photon transitions (**Paper III**, Fig. 3.2 B) and when $\hbar\Omega > I_p$ (**Paper I-II and IV-VI**, Fig. 3.2 A). From the intermediate state, an IR photon can either be absorbed (+) as shown in Fig. 3.2, or emitted (-), as indicated by the superscript of the two-photon transition matrix element.

Due to the finite nature of both the IR and the XUV pulses, the effects of the bandwidths must be included in our description of the two-photon ionization amplitude. Each energy of the final continuous state may be obtained by several pairwise combinations of IR and XUV frequencies, such that $\hbar(\Omega + \omega) = \epsilon_f - \epsilon_g = \hbar\Omega_{\epsilon_f g}$. The final two-photon transition amplitude is hence given by a convolution integral [73, 74],

$$A_{g,\epsilon_f}^{(\pm)}(\Omega_{\epsilon_f g}, \tau) = -\frac{ie^2}{\hbar} \int_0^\infty d\Omega \tilde{E}_{IR}(\Omega_{\epsilon_f g} - \Omega) e^{i(\Omega_{\epsilon_f g} - \Omega)\tau} \tilde{E}_{XUV}(\Omega) M_{g,\epsilon_f}^{(\pm)}(\Omega), \tag{3.2}$$

where $\tilde{E}_{IR}$ and $\tilde{E}_{XUV}$ are the spectral IR and XUV amplitudes, respectively, and τ is the delay between the two fields. The two-photon spectral signal $S(\epsilon_f, \tau)$, is proportional to the square of the final two-photon transition amplitude.

At high laser intensities, multiphoton ionization becomes possible as shown in Fig. 3.2 C. In this work however, intensities of the IR are kept low ($\approx 10^{11}$ W/cm^{-2}), such that multiphoton ionization does not readily occur.

3.1.3 Fano resonances

In **Paper II**, we study photoionization close to autoionization resonances, where a bound state is embedded in a continuum, interacts with it via the Coulomb interaction and auto-ionizes (see Fig. 3.3 A). This results in two different quantum paths to the same final energy which interfere with each other. These resonances exhibit a characteristic asymmetric profile (see Fig. 3.3), first described theoretically by Ugo Fano [75]. The resulting photoelectron wave-packet exhibits both amplitude and phase variations across the resonance, illustrated in Fig. 3.3 B.

Following the Fano formalism, the interaction of an atom with a single XUV photon populates a quasi-bound state, consisting of a superposition of an excited discrete bound state $|\alpha\rangle$ and a broadband continuum state $|\beta_\epsilon\rangle$ [75],

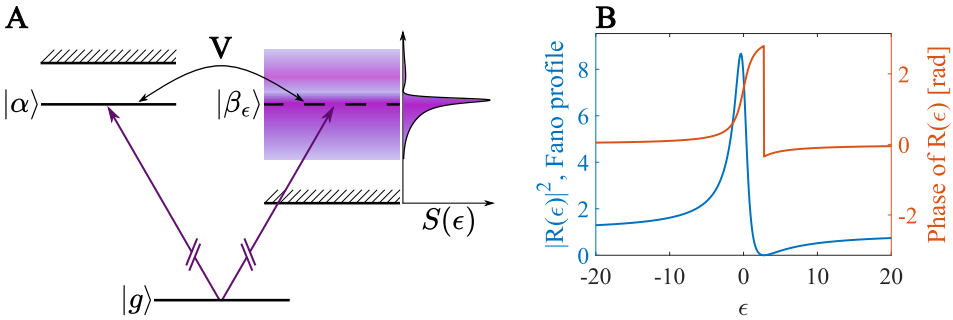

Figure 3.3: In A, we have the energy diagram of the 2s2p Fano resonance in helium with $q = -2.77$. In B, the Fano profile (in blue) and the phase (orange) of the resonance factor is presented.

$$|\Psi\rangle_e = \alpha\,|\alpha\rangle + \int d\epsilon\beta(\epsilon)\,|\beta_\epsilon\rangle\,, \tag{3.3}$$

where α and $\beta(\epsilon)$ are the complex coefficients of the bound and continuum states, respectively. The one-photon transition matrix element from the ground state $|g\rangle$ to the photoelectron state $|\Psi\rangle_e$ can be expressed as

$$\langle\Psi|_e\,\hat{z}\,|g\rangle = \langle\beta_\epsilon|\,\hat{z}\,|g\rangle\,\frac{q+\epsilon}{\epsilon+i}, \tag{3.4}$$

where $\epsilon = 2(E - E_\alpha)/\Gamma$ is the reduced energy, E_α, the resonance energy, $\Gamma = 2\pi|V|$, the width of the resonance and V characterizes the configuration interaction between the bound and continuum states. The Fano q parameter is a real number that characterizes the resonance, depending on the relative strength of the transition matrix elements of the autoionizing and direct ionization paths, as

$$q = \frac{\langle\alpha|\,\hat{z}\,|g\rangle}{\pi V^*\,\langle\beta_\epsilon|\,\hat{z}\,|g\rangle}. \tag{3.5}$$

The transition matrix element from the ground state to the photoelectron state (Eq. (3.4)), is simply the product of the transition matrix element to the unperturbed continuum, by the resonance factor

$$R(\epsilon) = \frac{q+\epsilon}{\epsilon+i}. \tag{3.6}$$

In the presence of a Fano resonance, the non-resonant spectral profile shown in Fig. 3.1, is modulated by the absolute square of the resonance factor, resulting in the characteristic asymmetrical Fano profile illustrated in Fig. 3.3. For $q = 0$, we have a symmetrical

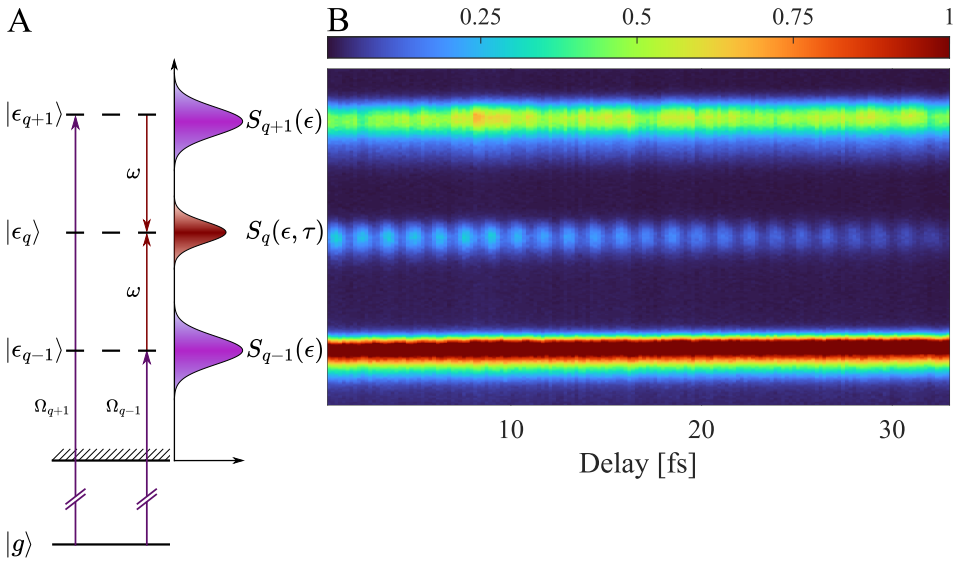

Figure 3.4: A, energy diagram of the RABBIT protocol, and B, an example of the photoelectron spectrum as a function of delay experimentally measured in helium.

window resonance with a decrease of the photoelectron signal around the resonance. In the limit of $q \to \pm\infty$, we recover a symmetric Lorentzian profile, typical for a bound transition. In **Paper II**, we study the $3s^1 3p^6 4p$ window resonance in argon in great detail, with $q = -0.25$ (see Section 3.3.1).

3.2 RABBIT

In order to resolve electron dynamics occurring on its natural timescale, interferometric protocols capable of accessing both the amplitude and phase of the emitted photoelectron wave-packet are used. In **Paper I-III**, all photoelectron measurements utilizes the RABBIT (Reconstruction of Attosecond Beating By Interference of Two-photon transitions) [13] protocol. RABBIT is based on conventional two-photon ionization processes, using a weak IR probe pulse in conjunction with an XUV APT, generated through HHG (see Section 2.2). The XUV APT consists of odd-order harmonics of the fundamental IR frequency, such that $\Omega_{q\pm1} = (q \pm 1)\omega$.

As shown in Fig. 3.4 A, two neighboring harmonics of orders $q \pm 1$, populate two continuum states $|\epsilon_{q\pm1}\rangle$, respectively. With the introduction of a weak IR probe pulse with frequency ω, additional transitions within the continuum through the absorption (+) or stimulated emission (-) of an IR photon are enabled, resulting in two-photon pathways to the same final energy state $|\epsilon_q\rangle$.

This leads to the appearance of three spectral features (see Fig. 3.4 B) in the total photoelectron spectrum. The first two are the spectra $S_{q\pm1}(\epsilon)$, generated by single-photon ionization of the atom by absorption of the XUV harmonic pulses, called main bands. The last one, referred to as a sideband (SB), is located between the two main bands spaced by $2\hbar\omega$. The SB arises from the interference of two quantum paths: the ionization by the absorption of harmonic $q-1$ followed by the absorption (+) of an IR photon, or the ionization by the absorption of harmonic $q+1$ followed by the stimulated emission (-) of an IR photon. The SB spectrum oscillates as a function of the delay τ, between the XUV and IR fields according to [61, 76],

$$S_q(\epsilon,\tau) = \left|A_{q-1}^{(+)}\right|^2 + \left|A_{q+1}^{(-)}\right|^2 + 2\left|A_{q-1}^{(+)}\right|\left|A_{q+1}^{(-)}\right|\cos(\Delta\Phi), \tag{3.7}$$

where $A_{q\mp1}^{(\pm)}$ are the two-photon transition amplitudes for the absorption (+) and emission (–) paths. The SB phase $\Delta\Phi$, can be decomposed into three individual contributions $\Delta\Phi = 2\omega\tau - \Delta\varphi_{\mathrm{XUV}} - \Delta\varphi_{\mathrm{A}}$. Assuming that the phase of the fundamental IR field is constant, the phase difference coming from the IR field is equal to $2\omega\tau$, where τ is the delay relative to the XUV. The second term is related to the XUV, and is equal to the phase difference between the two consecutive harmonics involved [61, 76],

$$\Delta\varphi_{\mathrm{XUV}} = \arg[E_{\mathrm{XUV}}(\Omega_{q+1})] - \arg[E_{\mathrm{XUV}}(\Omega_{q-1})] \approx 2\omega\tau_{\mathrm{XUV}}. \tag{3.8}$$

Here τ_{XUV} is the XUV group delay [61]. Lastly, the atomic phase difference

$$\Delta\varphi_{\mathrm{A}} = \arg[M_{g,\epsilon_q}^{(-)}(\Omega_{q+1})] - \arg[M_{g,\epsilon_q}^{(+)}(\Omega_{q-1})], \tag{3.9}$$

provides insight into the electron dynamics of the ionization process. By scanning over the delay and fitting the oscillations of each SB according to Eq. (3.7), one can extract the spectral variation of $\Delta\varphi_{\mathrm{XUV}} + \Delta\varphi_{\mathrm{A}}$. Assuming that we ionize into a flat, featureless continuum (as is the case in Fig. 3.4 B), this spectral variation, can largely be attributed to the group delay of an attosecond pulse in the train [13].

The RABBIT protocol does thus not only provide the means to retrieve the temporal structure of the ionizing APT, but also gives access to the temporal dynamics of the photoelectron wave-packets themselves [15]. This can be the study over a broad spectral range, with corresponding ultrafast attosecond dynamics [15, 17–19]. The RABBIT protocol has also been used to study the influence of resonances on the wave-packet such as in **Paper II** and **III**.

Sometimes the photoelectron state is created only is partly coherent, i.e. it cannot be described by the wavefunction formalism used in this section. In this case, one cannot readily apply the RABBIT protocol, but must instead utilize other methods such as Mixed-FROG [77], or KRAKEN described in **Paper IV-VI** and Section 4.

3.2.1 Rainbow RABBIT

Rainbow RABBIT is an energy-resolved extension of the RABBIT protocol, developed by Gruson et al. [25]. Unlike conventional RABBIT, where the SB signal is integrated over its spectral width, Rainbow RABBIT measures the phase across the width of the SB. This spectrally resolved measurement enables the reconstruction of the amplitude and phase of electron wave-packets with high energy-resolution. The protocol is particularly useful for studying fast phase variations within a SB arising from resonances (see **Paper II** and **III**). By fitting the SB oscillations as a function of the XUV–IR delay independently for each energy bin, Rainbow RABBIT provides detailed information on photoionization dynamics. However, the method relies on the assumption that the XUV chirp across the SB is negligible. In cases where femtochirp or blueshift effects are significant, additional corrections may be necessary to accurately extract phase information.

3.3 Experimental RABBIT measurements

3.3.1 Photoionization of argon close to the $3s^{-1}4p$ Fano resonance

In **Paper II**, we study the photoionization of argon atoms across the $3s^{-1}4p$ Fano resonance using the Rainbow RABBIT technique [25]. The upgraded setup described in Section 2.3 allows us to improve on studies previously made [24, 78], by fully spectrally resolving the two SO components ($\Delta\epsilon_{\mathrm{SO}}$ = 177 meV).

In Fig. 3.5 A, the energy diagram of the two-photon ionization scheme is presented. The presence of autoionizing states is shown on the left not only in the one-photon intermediate state, but also in the final two-photon states. The spectra as a function of pump-probe delay are shown for SB18 (B) and SB16 (C). The SO components are clearly resolved thanks to the narrow 10 nm probe bandwidth. The 2ω oscillations are extracted from the spectrograms and presented in D and E, respectively.

Fig. 3.6 shows the 2ω spectral amplitude (black) and phase (blue) for SB16 (A and C) and SB18 (B and D), using a 10-nm bandwidth probe (A and B) and a 35-nm bandwidth probe (C and D). A clear difference can be observed between SB16 (A) ex-

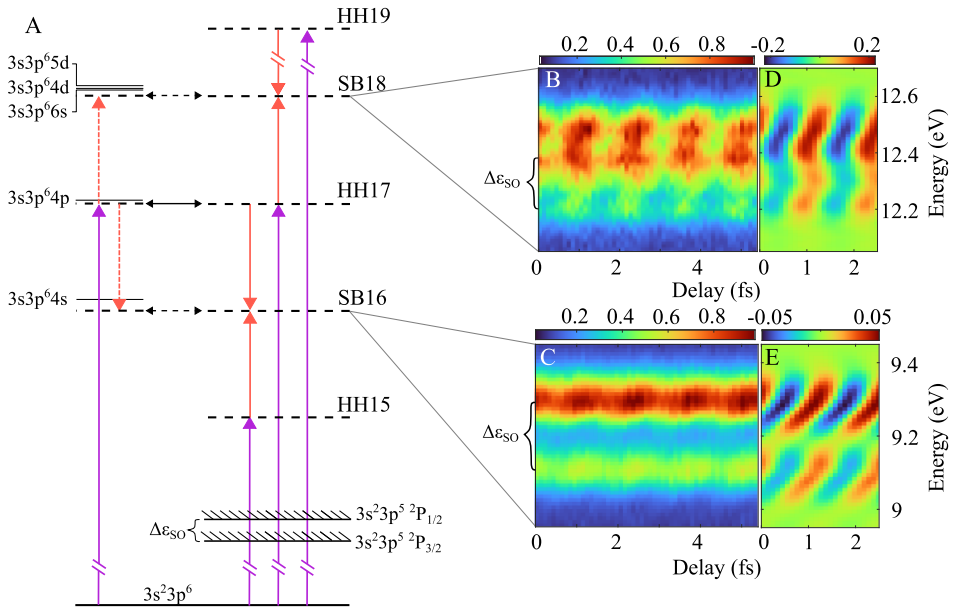

Figure 3.5: (A) Diagram showing the levels, channels, and processes involved in the experiment. Purple (red) arrows represent harmonic (IR) photon interactions. Black arrows indicate autoionization pathways. Dashed lines denote continuum or virtual states accessed through absorption of a harmonic photon or a combination of harmonic ± IR photons. Solid lines represent quasi-bound states that can decay via autoionization. (B) Measured photoelectron spectra in SB18, and (C) in SB16 in argon, plotted against the delay between XUV and IR pulses. (D) Photoelectron spectra in SB18 and (E) in SB16 after extracting the oscillations. Adapted from **Paper II**.

hibiting a 2π phase shift, while the variation of SB18 (B) is less than 1.4 rad. However, when both SB are measured instead with a 35-nm bandwidth probe (C and D), both phase variations are smoothed out and agree with previous measurements indicated in red [78].

The different phase variations of SB16 and SB18 can be modelled with the help of an effective complex q-parameter. We assume that the two-photon transition matrix element (see Eq. (3.1)) can be represented close to resonance as

$$M_{g,\epsilon_f}(\epsilon) \propto \frac{\tilde{q}+\epsilon}{\epsilon+i}, \tag{3.10}$$

where $\tilde{q}$ is the effective complex q-parameter. Fig. 3.7 shows the variation of M_{g,ϵ_f} in the complex plane (A and C) and its corresponding spectral phase (B and D). Different values of $\tilde{q}$, lead to different complex trajectories (Fig. 3.7 A) e.g. far from the origin (black), passing through the origin (blue), or enclosing the origin (red). The corresponding phase variations (B) are less than π, exactly π, and 2π, respectively. Due to finite pulse effects leading to a mixing of different spectral components, the complex

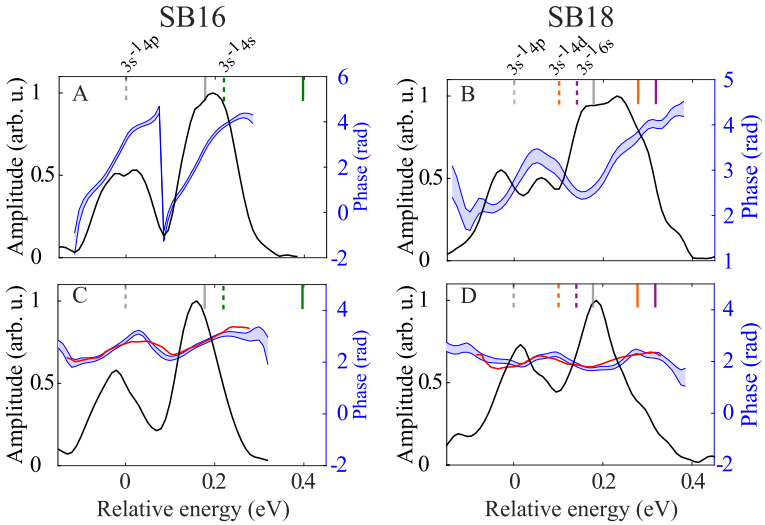

Figure 3.6: (A-D) Amplitude (black) and phase (blue) of SB16 and SB18 measured with 10 nm (A, B) and 35 nm (C, D) bandwidth probe. Red curves from Ref. [78] are offset for comparison. Vertical lines mark $3s^{-1}4s$ (green), $3s^{-1}4d$ (orange), $3s^{-1}6s$ (violet), and $3s^{-1}4p \pm 1$ IR photon (grey) resonance positions. Dashed and solid lines indicate the $^2P_{1/2}$ and $^2P_{3/2}$ ionic states, respectively. Adapted from **Paper II**.

two-photon transition amplitude shrinks as the bandwidth of the probe increases, making it possible to switch between including the origin or not, thus changing the phase variation.

A similar phase variation may also be found if we assume that the matrix element can be written as [24]

$$M_{g,\epsilon_f}(\epsilon) = M^{(0)}_{g,\epsilon_f}\frac{q+\epsilon}{\epsilon+i} + M^{(bg)}_{g,\epsilon_f} = (M^{(0)}_{g,\epsilon_f} + M^{(bg)}_{g,\epsilon_f})\frac{\tilde{q}+\epsilon}{\epsilon+i}, \tag{3.11}$$

where $M^{(i)}_{g,\epsilon_f}$ are the matrix components for the interacting (0) and non-interacting (bg=background) channels, and [79]

$$\tilde{q} = (qM^{(0)}_{g,\epsilon_f} + iM^{(bg)}_{g,\epsilon_f})/(M^{(0)}_{g,\epsilon_f} + M^{(bg)}_{g,\epsilon_f}). \tag{3.12}$$

This describes the case of an interacting continuum and a non-interacting one which arises in the case of several angular channels. Depending on the background (Fig. 3.7 C), the complex trajectory may lie far from the origin (black), pass through the origin (blue), or enclose the origin (red), corresponding to phase variations (D) of less than π, exactly π, and 2π, respectively.

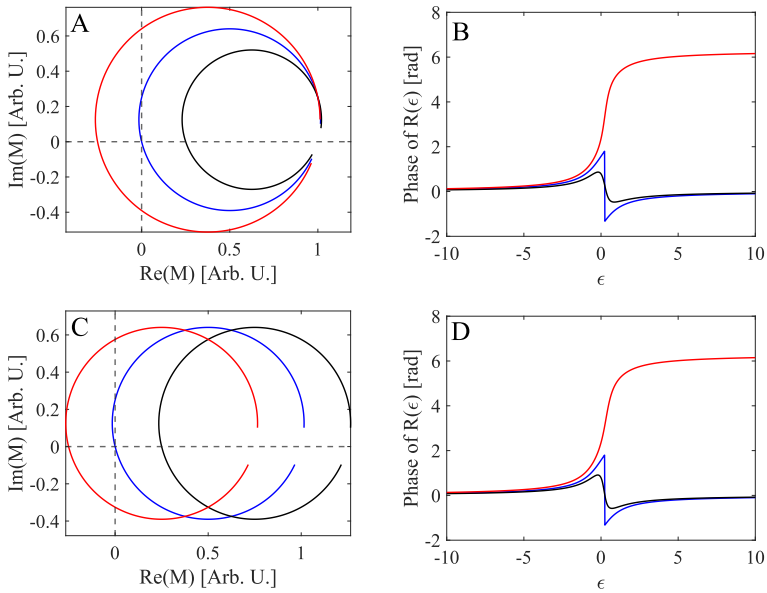

Figure 3.7: The complex two-photon matrix element $M(\omega)$ (A and C), and corresponding phase $\arg[M(\omega)]$ (B and D), (A-B) for the cases $\tilde{q}$ =–0.25+0.25i (black), $\tilde{q}$ = –0.25 (blue) and $\tilde{q}$ = –0.25-0.25i (red) and (C-D) without (blue), with positive (black), or negative (red) background. Adapted from **Paper II**.

Finally, a calculation presented in **Paper II** shows that the presence of resonances near the final state can result in final-state interactions that shift and/or elongate the complex trajectory in the complex plane, leading to a different phase variation for SB16 and SB18. This demonstrates that the narrowband RABBIT protocol is a highly sensitive tool, capable of revealing subtle quantum pathways that may otherwise be obscured by finite-pulse effects. A comprehensive understanding of resonances in both intermediate and final states is therefore essential, along with careful control over the probing conditions and their influence on the studied system.

3.3.2 Resonant photoionization of helium Rydberg states

In **Paper III**, we investigate two-photon resonant ionization of helium via intermediate states in the $1snp^1P_1$ Rydberg series with n = 3–5 (see Fig. 3.8). The IR frequency is tuned such that the 15th harmonic is resonant with the 3p, 4p and 5p states, followed by ionization due to the absorption of an additional IR photon. To probe the phase of the resulting electronic wave-packet, we use a non-resonant two-photon pathway leading to the same final state—namely, absorption of the 17th harmonic followed by stimulated emission of an IR photon, using the rainbow RABBIT technique. Angular-resolved combined with angular-integrated measurements (See Section 2.3.4), enable an extension of previous studies [23, 80].

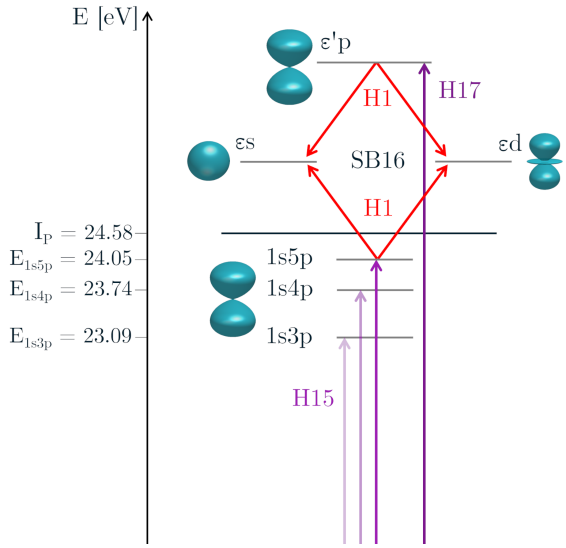

Figure 3.8: Energy levels and two-photon ionization pathways via the 3p, 4p, and 5p Rydberg states in helium. Violet and red arrows indicate excitation by the 15th and 17th harmonics and IR photons, respectively. The spherical harmonics corresponding to the different angular momentum channels are indicated in cyan. Adapted from **Paper III**.

Fig. 3.9 shows the angle-integrated spectral intensity and phase retrieved using the VMIS. In A, three broad maxima appear approximately at the positions of the $1snp^1P_1$ resonances for n = 3–5, from left to right. Note that the relative intensity strengths are arbitrary and not to scale. In B, the measured spectral phase (red line), is shown alongside simulations based on the Random Phase Approximation with Exchange (RPAE) [81], both without (grey dashed line) and with (black solid line) the inclusion of pulse bandwidth and power-induced broadening. A phase jump close to π is observed at each resonance. The slowly varying slope across the resonances is only reproduced when finite pulse effects are included (red and dashed grey lines). Additionally, phase jumps of opposite sign and similar magnitude appear between the resonances, corresponding to energies where the transition matrix elements vanish and change sign (these are called "antiresonances").

There are two final states with angular momenta s or d and different angular probability distributions. Simulations of the contributions of the angular channels around the 4p resonance were performed and the phase variations as a function of energy and angle are presented in Fig. 3.10 B. As expected, both s- and d-channels exhibit a sharp phase jump close to π rad due to the 4p-resonance (red), so that angle-integrated measurements are sufficient to capture on-resonance phase jumps. Both channels individually exhibit another clear phase jump due to an antiresonance, in the s-channel (right) at a lower kinetic energy (blue), and in the d-channel (left) at a higher kinetic

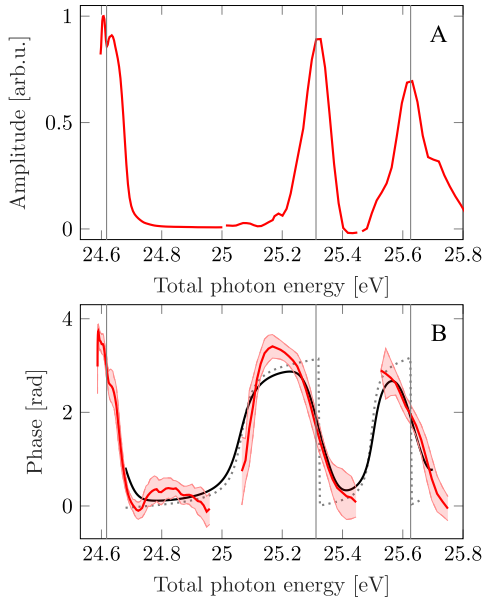

Figure 3.9: Two-photon ionization via 1snp states with n = 3, 4, 5. (A) Angle-integrated yield, with the red line representing experimental measurements and the black line showing results from RPAE-based simulations [81] and (B) angle-integrated phase. The red solid line indicates the measured data and the shaded regions reflect the uncertainty of the weighted average. Simulated phases are shown both without (grey dashed line) and with (black solid line) the inclusion of pulse bandwidth and power-induced broadening. Vertical grey lines mark the energies of the resonances for n = 3, 4, and 5. Adapted from **Paper III**.

energy (green). Further, the d-channel clearly exhibits an angular-dependent phase jump at the *magic angle* $\theta = 54.7°$. This angle corresponds to a zero of the spherical harmonic Y_{20}.

Fig. 3.10A (left) shows the total simulated phase of SB16 where contributions from all angular momentum channels are added. Due to the distinct angular and spectral dependencies of the phase for the contributing channels, the total SB16 phase exhibits smoother phase transitions at the anti-resonances, a pronounced phase jump at the 4p resonance, and a spectrally-dependent phase variation along the magic angle. Both the simulation and experiment confirms that the d-channel contribution dominates. The theoretical results are in good agreement with the experimentally retrieved phase data shown in Fig. 3.10A (right). Unfortunately, the experimental data could be reliably retrieved only over a small angle-energy region.

We also performed angle-integrated measurements using the MBES together with the newly implemented high-resolution setup (**Paper I** and Section 2.3). In Fig. 3.11 A, SB16 and H17 spectra are presented as a function of pump-probe delay. In B, the spectral phase across close to the 4p resonance is presented. The experimentally measured phase (dashed) is compared to the theoretically retrieved phase (solid) for

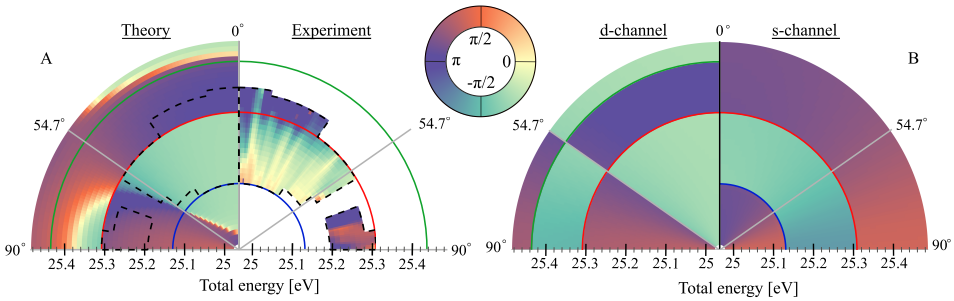

Figure 3.10: Angle- and energy-resolved relative phase of SB16 around the 4p resonance. (A) Comparison between experimental data (right) and theoretical simulation (left). Only regions with a sufficient signal over noise ratio are shown in the experimental panel, as indicated by the black dashed contour. The radial coordinate represents the total electron energy, while the polar angle corresponds to the electron emission angle relative to the laser polarization axis. The phase is encoded using the cyclic color scale shown in the top right corner. (B) Simulated contributions of the *s* (right) and *d* (left) waves in the absorption path. Adapted from **Paper III**.

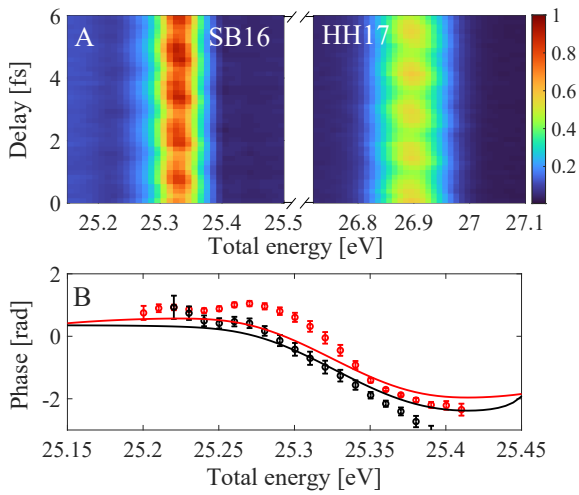

Figure 3.11: Angle-integrated measurements using MBES. (A) Spectra of SB16 and H17 as a function of pump-probe delay. (B) Extracted phase of SB16 for parallel (red) and perpendicular (black) polarizations, i.e. the d-wave only. Measured data (dashed lines) are compared with simulations (solid lines). Adapted from **Paper III**.

parallel XUV and IR polarization (red), where both s- and d-channels contribute, and perpendicular polarizations (black), where only the d-channel contributes (see **Paper III**). As expected, the π phase jump is clearly visible in both polarization configurations, confirming that the 4p resonance is resolvable in angle-integrated experiments. Here, the smooth jump can once again be understood by finite pulse effects.

Angle-integrated and angle-resolved measurements complement each other in revealing resonant ionization dynamics in helium. While integrated data capture clear π-phase shifts at resonance, angle-resolved measurements uncover channel-specific fea-

tures like anti-resonances and angular-dependent phase behavior. Their agreement confirms that both methods together provide a more complete and accurate characterization of the photoionization process.

Chapter 4

KRAKEN

In this chapter the KRAKEN protocol (Swe: **K**vanttillstånds tomog**R**afi av **A**ttose**K**und **E**lektro**N**vågpaket, Eng: quantum state tomography of attosecond electron wave-packet) is presented.

The chapter is divided into three parts. In Section 4.1 we describe the theoretical framework behind the KRAKEN protocol, initially presented in more detail in **Paper IV**. In Section 4.2, we present experimental measurements of the density matrix of photoelectrons created in helium and argon. Here we summarize some of the main conclusions and limitations presented in **Paper V**. Section 4.3 discusses an alternative QST protocol named Poly-KRAKEN, that generalizes the KRAKEN scheme for a more efficient reconstruction of the photoelectron density matrix as presented in **Paper VI**.

4.1 Theory of the KRAKEN protocol

The KRAKEN protocol is a quantum state tomographic (QST) measurement of a photoelectron created when an atom absorbs a short XUV pulse. Fig. 4.1 A schematizes the ionization of a neutral atom with a pulse with a central frequency Ω and spectral width $\delta\Omega$ leading to a spectrally broad photoelectron wave-packet. The quantum state representing the ion and the photoelectron can be written as

$$|\Psi\rangle_{Ie} = \int d\epsilon \sum_j c_j(\epsilon)\, |j\rangle_I \otimes |\epsilon\rangle_e \,, \tag{4.1}$$

where $c_j(\epsilon)$ are complex coefficients ($\int d\epsilon \sum_j \left|c_j(\epsilon)\right|^2 = 1$), $|\epsilon\rangle_e$ are the continuum states, which we label with their energy ϵ, and $|j\rangle_I$ are the ionic states which we label with their degrees of freedom j. The combined system described in Eq. (4.1) is known as a *bipartite* system (ion-electron). If this bipartite state can be written as a tensor product of the individual contributing state vectors, i.e. $|\Psi\rangle_{Ie} = |\Psi\rangle_I \otimes |\Psi\rangle_e$, then the state is defined as *separable*. Any pure bipartite state that cannot be written as tensor product of the individual contributing state vectors, i.e. is not separable, is then *entangled* [82]. In other terms, unlike separable states where the information of each individual physical system can be understood without knowledge of the whole bipartite system, for an entangled system this is not the case. For an entangled state, one cannot measure one subsystem without affecting the other subsystem as well.

Since we only measure the photoelectron, we have to trace over the ionic degrees of freedom. Assuming that we have an initial pure state, we end up with a final expression of the photoelectron density matrix [**Paper IV**]

$$\rho_e = tr_I(|\Psi_{Ie}\rangle\langle\Psi_{Ie}|) = \int d\epsilon_1 d\epsilon_2 \sum_j c_j(\epsilon_1) c_j(\epsilon_2)^* |\epsilon_1\rangle\langle\epsilon_2| . \tag{4.2}$$

The purity of the reduced photoelectron state is defined as [**Paper V**]

$$\gamma = Tr(\rho_e^2) = \int d\epsilon_1 d\epsilon_2 \left|\rho_e(\epsilon_1, \epsilon_2)\right|^2 . \tag{4.3}$$

A pure state is defined such that $\gamma = 1$, and for $\gamma < 1$, we have what is known as *mixed state*. As the name suggests, mixed states can be understood as an incoherent mixture of pure states, thus implying that the total photoelectron state is partially coherent [82, 83].

The photoelectron spectrum, $S(\epsilon)$, measured with the MBES (see Fig. 2.15) or similar spectrometers, only gives access to the main diagonal of the density matrix, as illustrated in Fig. 4.1 D. Fig. 4.1 presents the energy diagram of the ionization process (A) and the corresponding elements of the density matrix obtained from the photoelectron spectrum (D). These elements of the density matrix are known as the *populations*. Since the photoelectron state is broadband and continuous, its density matrix will also be broadband and continuous. For illustrative purposes, we present the density matrix composed of discrete elements, as in an experimental measurement.

To characterize the entire density matrix, we must also retrieve the off-diagonal elements, called *coherences*. This can be done as illustrated in Fig. 4.1 B, by the utilization of a bichromatic probe, composed of phase-locked synchronized spectral components, ω_1 and ω_2. As such, two intermediate states, $|\epsilon_1\rangle$ and $|\epsilon_2\rangle$, can be coupled to the

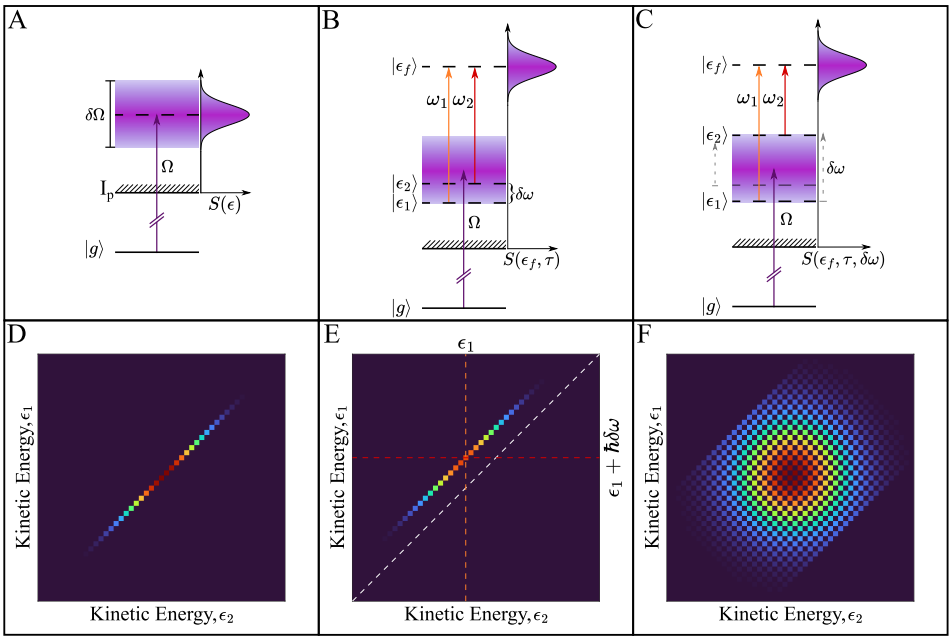

Figure 4.1: An illustration of the KRAKEN protocol. In A to C, the energy diagrams for different ionization protocols are represented. In D to F, density matrix elements are indicated, where elements in dark blue represent elements not retrieved. In A and D, the photoelectron spectrum $S(\epsilon)$, is due to single-photon ionization of an atom from its ground state $|g\rangle$, to a broad spectral region of the ionization continuum. In B and E, the photoelectron spectrum $S(\epsilon_f, \tau)$, results from two-photon ionization, due to the XUV and a bichromatic probe field, projecting two different spectral components, $|\epsilon_1\rangle$ and $|\epsilon_2\rangle$, of the intermediate photoelectron state to the same final state, $|\epsilon_f\rangle$, allowing the retrieval of a sub-diagonal of the density matrix. And finally, in C and F, the photoelectron spectrum $S(\epsilon_f, \tau, \delta\omega)$, is obtained by scanning the bichromatic separation, $\delta\omega$, over the width of the photoelectron state, $\delta\Omega$, allowing the retrieval of a sparse density matrix.

same final state, $|\epsilon_f\rangle$, such that $\epsilon_f = \epsilon_1 + \hbar\omega_1 = \epsilon_2 + \hbar\omega_2$. As described in **Paper IV**, the photoelectron spectrum corresponding to the absorption of an XUV pulse and a bichromatic probe field delayed by τ, can be approximated to:

$$\begin{aligned} S(\epsilon_f, \tau) \approx &\left|\mu_{\epsilon_f,\epsilon_1}\right|^2 \rho_e(\epsilon_1, \epsilon_1) + \left|\mu_{\epsilon_f,\epsilon_2}\right|^2 \rho_e(\epsilon_2, \epsilon_2) \\ &+ e^{i\delta\omega\tau} \mu_{\epsilon_f,\epsilon_1} \mu^*_{\epsilon_f,\epsilon_2} \rho_e(\epsilon_1, \epsilon_2) + e^{-i\delta\omega\tau} \mu_{\epsilon_f,\epsilon_2} \mu^*_{\epsilon_f,\epsilon_1} \rho_e(\epsilon_2, \epsilon_1), \end{aligned} \tag{4.4}$$

where $\delta\omega = \omega_1 - \omega_2 = (\epsilon_2 - \epsilon_1)/\hbar$ and $\mu_{\epsilon_f,\epsilon_i}$ are dipole transition matrix elements between continuum states, $|\epsilon_{1,2}\rangle$ and $|\epsilon_f\rangle$. Only the terms in the second line in Eq. (4.4) oscillate with a beating frequency of $\delta\omega$ with the pump-probe delay, hence the coherences are easily obtained. These coherences are represented in Fig. 4.1 E and the location of a single density matrix element $\rho_e(\epsilon_1, \epsilon_1 + \hbar\delta\omega)$, is clarified with

the orange and red dotted lines. For a single $\delta\omega$, all the coherences corresponding to intermediate continuum states separated by $\delta\omega$ will be measured. We therefore obtain not only a single off-diagonal element but a full sub-diagonal (Fig. 4.1 E). Additionally, since the density matrix is hermitian $\rho_e(\epsilon_1, \epsilon_2) = \rho_e^*(\epsilon_2, \epsilon_1)$, only half of the density matrix needs to be measured. As such, the same sub-diagonal is also present under the main diagonal with the same separation (not shown).

In order to reconstruct the sparse density matrix, one needs a series of unique projective measurements on the photoelectron state. This method is known as QST and is the gold standard for characterization of a quantum state as covered in [**Paper IV**]. For each $\delta\omega$, one sub-diagonal is obtained from the analysis of the photoelectron spectrum, $S(\epsilon_f, \tau)$. By scanning $\delta\omega$ over the width of the photoelectron state $0 \leq \delta\omega \leq \delta\Omega$, and measuring $S(\epsilon_f, \tau, \delta\omega)$, one can obtain several sub-diagonals, as illustrated in Fig. 4.1, C and F. The sparse density matrix is therefore retrieved directly from measurements, without relying on an retrieval algorithm, with an arbitrary energy resolution. Note that the density matrix is "sparse" since it is obtained from a discrete number of measurements.

4.2 Experimental KRAKEN measurements

In **Paper V**, KRAKEN measurements are performed in helium and argon. In both experiments we ionize the target gas using the 19^{th} harmonic generated in argon ($\hbar\Omega \approx 29.4$ eV), with a spectral width of $\hbar\Omega = 140$ meV. While the ion and the photoelectron form a simple bipartite product state in helium, this is not necessarily the case for argon. As illustrated in Fig. 4.2, the ionic ground state in argon is split into two states due to SO splitting, separated by $\Delta\epsilon_{\mathrm{SO}} \approx 177$ meV. The final state in argon is therefore a sum of two ion-electron product states, where the ion can be in the $^2P_{1/2}$ or $^2P_{3/2}$ states. In Subsection 4.2.1, we will present the experimental method and the main results in helium. In Subsection 4.2.2 we will focus on the results obtained in argon, and how the SO splitting affects the purity.

4.2.1 Measurements in helium

Performing a full KRAKEN measurement is quite challenging, since it requires about a full hour for each sub-diagonal and an additional two for the main diagonal. Further, for the entire duration of the experiment, a high laser stability is required. The setup used for the measurements is presented in detail in Section 2.3 (see also Fig. 2.11). One spectral component of the probe was kept fixed at 770 nm, while the other spectral component was tuned between 790-840 nm in steps of 10 nm. The bandwidth of

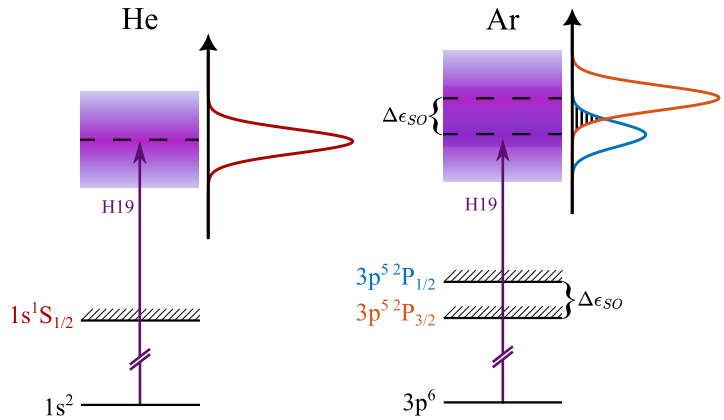

Figure 4.2: Illustration of the ionization process and photoelectron spectrum in helium and argon. In argon, two spectral peaks (orange and blue) separated by the SO splitting, $\Delta\epsilon_{SO} = 177$ meV, with different statistical weights are shown. These two states may spectrally overlap depending on the width of the individual photoelectron states.

each spectral component of the probe was equal to 8 nm.

The measurements in helium are presented in Fig. 4.3 A. Each column corresponds to a different $\delta\omega$, varying between 0 (left) and 134 meV (right). The sub-diagonal amplitude, $A_{\delta\omega}(\epsilon_1) \propto \rho_e(\epsilon_1, \epsilon_1 + \hbar\delta\omega)$, and phase, $\theta_{\delta\omega}(\epsilon_1) = arg[\rho_e(\epsilon_1, \epsilon_1 + \hbar\delta\omega)]$ were extracted through a fit to the oscillations (Fig. 4.3 A), using a cosine function with a Gaussian envelope. Instead of using XUV-only photoelectron spectrum as presented in Fig. 4.1 A [71], we determine the main diagonal through a two-photon process to maintain the relative amplitude between the main and sub-diagonals. We obtain $A_0(\epsilon_1)$ (proportional to $\rho_e(\epsilon_1, \epsilon_1)$), by blocking a single spectral component of the otherwise bi-chromatic probe. A shutter allows us to record the background noise which is then subtracted out to improve the signal-to-noise ratio since the main diagonal is more affected by static noise. The retrieved amplitudes $A_{\delta\omega}$ are shown in Fig. 4.3 B.

Since the central frequency is different for different $\delta\omega$, the amplitude $A_{\delta\omega}$ are slightly shifted in energy with respect to each other. This shift must be compensated when building the sparse density matrix. We also take into account small Stark shifts (see supplemental information of **Paper V**). Both the harmonic and probe spectra are recorded and used to normalize the retrieved amplitudes according to

$$\rho_e(\epsilon_1, \epsilon_1 + \delta\omega) = \frac{A_{\delta\omega}(\epsilon_1)}{I_H \sqrt{I_{\omega_1} q_{\omega_1} I_{\omega_2} q_{\omega_2}}}, \tag{4.5}$$

where I_H, I_{ω_1} and I_{ω_2} are the integrated spectral intensities of the harmonic and the

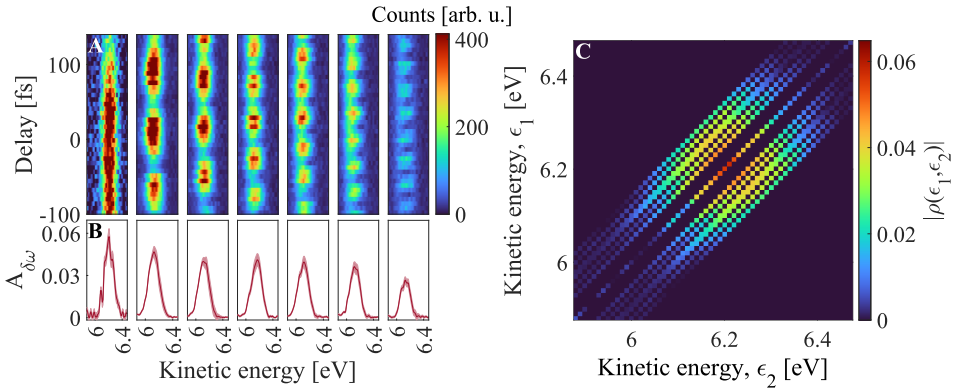

Figure 4.3: A, photoelectron spectrograms acquired for different values of $\delta\omega$ (from left to right: $\hbar\delta\omega$ = 0, 41, 61, 80, 98, 117, 134 meV). B, energy-resolved oscillation amplitudes, $A_{\delta\omega}$, extracted from the same spectrograms. C, the density matrix obtained by inserting the oscillation amplitudes for each $\delta\omega$ at the corresponding position. The dark blue areas correspond to regions of the density matrix that are not reconstructed. Adapted from **Paper V**.

two spectral components respectively, and q_{ω_1} and q_{ω_2} are the relative spectrometer responses at ω_1 and ω_2 respectively. The elements of the density matrix are further scaled so that the trace of the density matrix is equal to 1. The sparse density matrix obtained in helium is finally presented in Fig. 4.3 C. It is worth mentioning that the gap between the main- and sub-diagonals is simply due to experimental constraints. In our measurements, the smallest $\delta\omega$ was limited by how close we can place the two slits in the 4f-shaper, see Fig. 2.12.

Retrieving the full density matrix from the measured sparse density matrix is a non-trivial problem. In **Paper V** we employ a Bayesian estimation using a Hamiltonian Monte Carlo method [84]. The retrieved full density matrix is shown in Fig. 4.4 A. Similar to the measured sparse density matrix, the full density matrix is slightly elongated along the main diagonal. This observation is due to the energy resolution of the spectrometer, see Eq. 2.15, as originally discussed in [35] and in appendix E of **Paper IV**. However, by measuring the point-spread function and taking it into account in the Bayesian estimation protocol, the retrieval of the original full density matrix is possible as shown in Fig. 4.4 B.

By retrieving the photoelectron density matrix and comparing it with theoretical simulations, the fidelity of the KRAKEN method can be computed. In **Paper V**, theoretical calculations using the Relativistic Random Phase Approximation with Exchange (RRPAE) are described [85]. As explained in Section 4.1, a direct single photon measurement of the photoelectron density matrix is not experimentally possible, but it is possible to theoretically simulate this density matrix. The mutual fidelity [86] of the single photon RRPAE density matrix ρ_1 and the experimentally retrieved density matrix ρ_{exp}, defined as

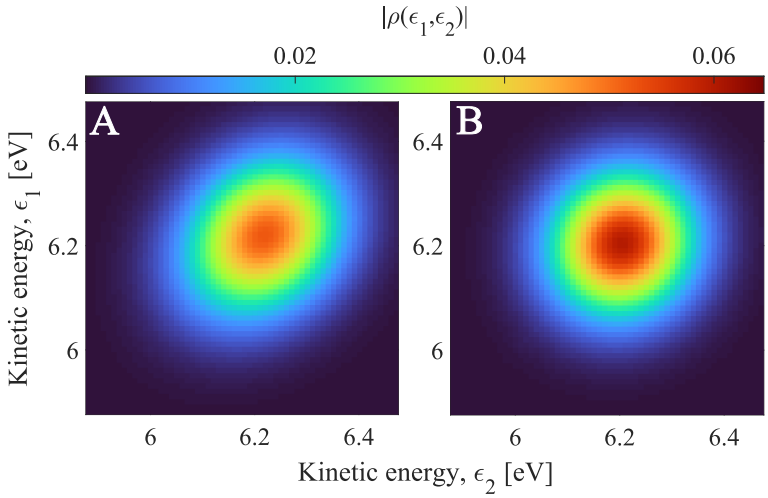

Figure 4.4: Density matrices in helium retrieved through Bayesian estimation using a Hamiltonian Monte Carlo method. A, the retrieval directly from experimental measurements resulting in an ellipsoid. The elongation along the main-diagonal is a known consequence due to the energy resolution of the MBES. B, the full density matrix obtained by eliminating its influence, indicates an almost fully pure state as expected. Adapted from **Paper V**.

$$F(\rho_{exp},\rho_1) = Tr\left[\left(|\rho_1|^{1/2}|\rho_{exp}|^{1/2}|\rho_1|^{1/2}\right)^{1/2}\right], \tag{4.6}$$

is found to be equal to 0.98. It shows that we can accurately retrieve the photoelectron density matrix with the KRAKEN method.

In Tab. 4.1, we compare the purities obtained in helium experimentally (γ_{exp}), and through single (γ_1) and two-photon (γ_2) RRPAE calculations, the latter simulating the KRAKEN protocol.

Table 4.1: Purity of the photoelectron state created from helium. From experiment (γ_{exp}), single photon calculations (γ_1) and simulations based on the KRAKEN protocol (γ_2). Adapted from **Paper V**.

	Experiment, γ_{exp}	Single-photon RRPAE, γ_1	KRAKEN RRPAE, γ_2
Helium	0.94 ± 0.06	1	1

The high measured purity can be understood by considering the bipartite state created by photoionization of helium, see Eq. (4.1) and Fig. 4.2,

$$|\Psi\rangle_{Ie} = \int d\epsilon\, c_{1/2}(\epsilon)\,|1/2\rangle_I \otimes |\epsilon\rangle_e = |1/2\rangle_I \otimes \int d\epsilon\, c_{1/2}(\epsilon)\,|\epsilon\rangle_e\,, \tag{4.7}$$

where $|1/2\rangle$ denotes the ionic state with the ionic angular momentum of $j = 1/2$. It is clear from Eq. (4.7), that we have a product state, i.e. the ion and electron states

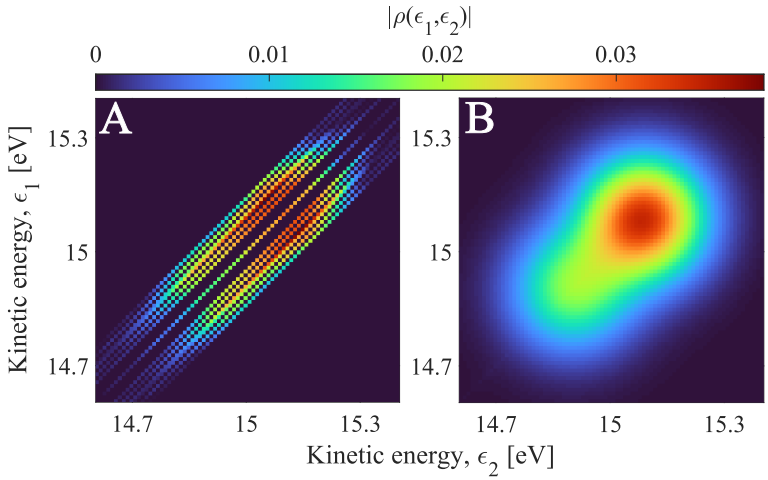

Figure 4.5: Sparse density matrix measured in argon (A) and the retrieved full density matrix after deconvolution (B). Adapted from **Paper V**.

are separable. Tracing over the ionic degrees of freedom we obtain

$$\rho_e = \int d\epsilon_1 d\epsilon_2 c_{1/2}(\epsilon_1) c^*_{1/2}(\epsilon_2) \left|\epsilon_1\right\rangle \left\langle\epsilon_2\right| . \tag{4.8}$$

Note that the notation for the ion and electron states is omitted when referring to the reduced photoelectron matrix. The photoelectron state is a pure state, and henceforth the purity is

$$\gamma = \int d\epsilon_1 d\epsilon_2 \left| c_{1/2}(\epsilon) \right|^2 = 1. \tag{4.9}$$

The theoretical obtained purities are equal to one and the experimental purity is very close to one, conveying the ability of the KRAKEN protocol to measure the photoelectron density matrix with minimal experimental decoherence.

4.2.2 Measurements in argon

Similar experiments were performed in argon and the results were analyzed as described above. Fig. 4.5 A shows the measured sparse density matrix, while B presents the full de-convolved density matrix retrieved through Bayesian estimation. The density matrix has an oval form, with a higher probability density at higher energies. The oval form shows that the argon photoelectron is in a mixed state.

The measured purity for argon is compared to the single photon and the two-photon theoretical calculations (based on RRPAE) in Tab. 4.2.

Table 4.2: Purity of the photoelectron state created from argon. Adapted from **Paper V**.

	Experiment, γ_{exp}	Single-photon RRPAE, γ_1	KRAKEN RRPAE, γ_2
Argon	0.65 ± 0.02	0.61	0.66

The experimental purity is equal to 0.65, in good agreement with the prediction of the theoretical calculations. In argon, the final state is a sum of two different contributions depending on the angular momentum of the ion state (see in Fig. 4.2),

$$\begin{aligned} |\Psi\rangle_{Ie} =& \int d\epsilon\, c_{1/2}(\epsilon)\, |1/2\rangle_I \otimes |\epsilon\rangle_e + \int d\epsilon\, c_{3/2}(\epsilon)\, |3/2\rangle_I \otimes |\epsilon\rangle_e \\ =& a_{1/2}\, |1/2\rangle_I \otimes \int d\epsilon\, b_{1/2}(\epsilon)\, |\epsilon\rangle_e + a_{3/2}\, |3/2\rangle_I \otimes \int d\epsilon\, b_{3/2}(\epsilon)\, |\epsilon\rangle_e \end{aligned} \tag{4.10}$$

where $c_j(\epsilon) = a_j b_j(\epsilon)$ and a_j and $b_j(\epsilon)$ are the complex coefficients characterizing the ion and electron states, respectively. In contrast to helium (see Eq. (4.7)), this state is not separable, but entangled when $b_{1/2}(\epsilon) \neq b_{3/2}(\epsilon)$. Note that $|a_{1/2}|^2$ and $|a_{3/2}|^2$ represent the statistical weights, 1/3 and 2/3 [87], for the two ionic angular momenta, respectively. Tracing over the ionic degrees of freedom, see Eq. (4.2), we obtain [**Paper V**]

$$\begin{aligned} \rho_e =& \frac{1}{3} \int d\epsilon_1 d\epsilon_2\, b_{1/2}(\epsilon_1) b^*_{1/2}(\epsilon_2)\, |\epsilon_1\rangle \langle\epsilon_2| \\ &+ \frac{2}{3} \int d\epsilon_1 d\epsilon_2\, b_{3/2}(\epsilon_1) b^*_{3/2}(\epsilon_2)\, |\epsilon_1\rangle \langle\epsilon_2| \,. \end{aligned} \tag{4.11}$$

Assuming that $b_{3/2}(\epsilon) = b_{1/2}(\epsilon - \Delta\epsilon_{\mathrm{SO}})$, where $\Delta\epsilon_{SO}$ is the SO split in energy for argon,

$$\begin{aligned} \rho_e =& \frac{1}{3} \int d\epsilon_1 d\epsilon_2\, b_{1/2}(\epsilon_1) b^*_{1/2}(\epsilon_2)\, |\epsilon_1\rangle \langle\epsilon_2| \\ &+ \frac{2}{3} \int d\epsilon_1 d\epsilon_2\, b_{1/2}(\epsilon_1 - \Delta\epsilon_{\mathrm{SO}}) b^*_{1/2}(\epsilon_2 - \Delta\epsilon_{\mathrm{SO}})\, |\epsilon_1\rangle \langle\epsilon_2| \,. \end{aligned} \tag{4.12}$$

As can be seen in (4.12), the photoelectron in argon can be described as a mixed state. This is due to an incomplete measurement over all degrees of freedom and the initial

entanglement between the ion and photoelectron (Eq. (4.10)). The purity can be expressed as

$$\gamma = \frac{5}{9} + \frac{4}{9}\left| \int d\epsilon \; b_{1/2}(\epsilon) b^*_{1/2}(\epsilon - \Delta\epsilon_{\mathrm{SO}}) \right|^2 . \tag{4.13}$$

The integral in Eq. (4.13) represents the overlap between the two photoelectron states created as illustrated Fig. 4.2. The ion and photoelectron are entangled for unless $\hbar\Omega$ is much larger than $\Delta\epsilon_{SO}$. The larger the XUV bandwidth, the larger the overlap becomes. When $b_{1/2}(\epsilon) \approx b_{1/2}(\epsilon - \Delta\epsilon_{\mathrm{SO}})$, $\gamma = 1$. In this case we recover a separable state and the argon photoelectron state is a pure state similar to helium; No information on the ionic state can be obtained by measuring the photoelectron state. In contrast, where the overlap is equal to zero, we have $\gamma = 5/9 \approx 0.56$. By measuring the photoelectron state, the wavefunction collapses, and we obtain full knowledge of the corresponding ionic state. The entanglement due to the SO interaction decreases as the overlap increases (see **Paper IV**). In the case studied in **Paper V** and detailed here, the overlap is between these two extremes, the entanglement is only partial and the purity is 0.65.

In conclusion, we have shown that KRAKEN is a very reliable method for measuring the quantum state of the photoelectron created by the ionization of a neutral atom.

4.2.3 Comparison between KRAKEN and Mixed-FROG

Another method for QST of photoelectrons generated by absorption of XUV pulses is Mixed-FROG (Frequency-Resolved Optical Gating for partially coherent (mixed) states), first proposed in [77] and later experimentally demonstrated in [35]. Mixed-FROG reconstructs the quantum state of a photoelectron created by the absorption of an attosecond pulse in a train, by measuring interference between multiple CC transitions driven by a strong IR field. By scanning the delay between an APT and an intense IR pulse, a high-frequency modulated spectrogram is recorded. The two protocols present important differences. The photoelectron state reconstructed in Mixed-FROG is created by absorption of an APT, whereas KRAKEN reconstructs the density matrix of a photoelectron created by absorption of a single harmonic.

Mixed-FROG relies on interference between quantum paths involving multiple CC transitions, which oscillate at high frequencies. As a result, it requires intense IR fields to induce these oscillations and extract coherence information. In contrast, KRAKEN uses a weak bichromatic IR field to perturb the ionization process and induce interference between selected energy levels in the final state. This allows the IR field to be treated perturbatively, a key advantage of KRAKEN.

In terms of experimental complexity, the Mixed-FROG setup requires minimal modification from a standard RABBIT setup, making it relatively easy to implement. By contrast, KRAKEN requires a more elaborate setup, including spectral tuning and selection of a bichromatic IR probe field, as detailed in Section 2.3 and above. The purities measured in [35] are of the order of 10^{-1}, most probably due to limited spectral-resolution and temporal instability. In KRAKEN, the signal is retrieved from lower oscillation frequencies, corresponding to a longer oscillation period and less requirements for temporal stability than both RABBIT and Mixed-FROG.

Finally, the data analysis approach differs significantly. Mixed-FROG relies on a retrieval algorithm (a generalized projection method that involves a physical model) to reconstruct the full density matrix. KRAKEN, on the other hand, extracts subdiagonals of the density matrix directly from the measured spectrogram. These must be acquired individually, requiring a series of measurements and thus increasing experimental time. The Poly-KRAKEN extension presented below significantly reduces the number of required measurements.

4.3 Poly-KRAKEN

We present a generalization of the KRAKEN protocol with a poly-chromatic probe field, allowing us to reduce the needed number of measurements. Eq. (4.4) can be generalized to more than two spectral components,

$$\begin{aligned} S(\epsilon_f, \tau) &\approx \sum_{j=1}^{n} \sum_{k=1}^{n} e^{i\tau(\omega_j - \omega_k)} \mu_{\epsilon_f,\epsilon_j} \mu^*_{\epsilon_f,\epsilon_k} \rho_e(\epsilon_j, \epsilon_k) \\ &= \sum_{j=1}^{n} \left|\mu_{\epsilon_f,\epsilon_j}\right|^2 \rho_e(\epsilon_j, \epsilon_j) + \sum_{\substack{j,k \\ j \neq k}} e^{i\tau\delta\omega_{jk}} \mu_{\epsilon_f,\epsilon_j} \mu^*_{\epsilon_f,\epsilon_k} \rho_e(\epsilon_j, \epsilon_k), \end{aligned} \tag{4.14}$$

where ω_i are the spectral frequencies of the probe, for j and k between 1 and n and $\delta\omega_{jk} = \omega_j - \omega_k$. As before, we can separate this equation into two parts, one including the n populations ($j = k$), one from each spectral component, and the other one including the $n^2 - n$ coherences ($j \neq k$). By increasing the amount of spectral components one does not simply get a linear increase in the number of coherences, but a quadratic one. This illustrates the clear benefit of having many spectral components for a KRAKEN scan, i.e. a poly-chromatic KRAKEN. However, the probe frequencies (ω_i) have to be carefully chosen in order to both cover as much as possible of the density matrix and to ensure that the resulting coherences are retrievable.

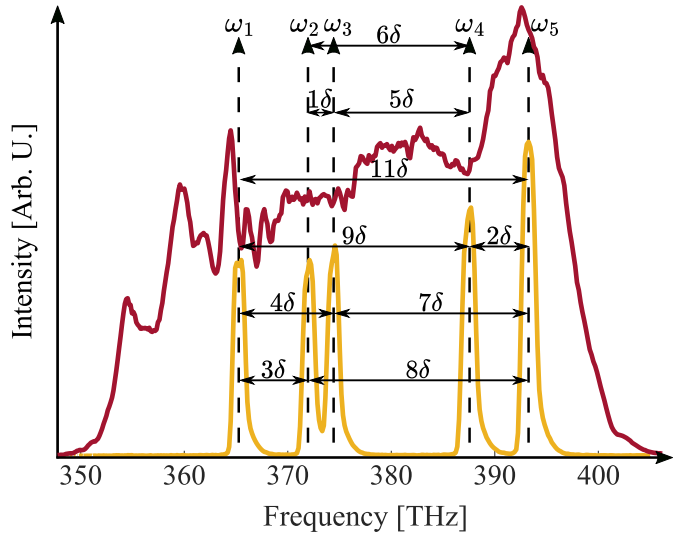

Figure 4.6: Probe spectrum before (red) and after (yellow) the 4f-shaper. A solution to the 5-slit Golomb ruler is presented with spectral peaks centered at $\omega_1 + ...[0, 3\delta, 4\delta, 9\delta, 11\delta]$. For this solution, all beating frequencies but 10δ are present between 1δ and 11δ. Adapted from **Paper VI**.

The key to solving this problem lies in breaking the symmetry in the spacing between the spectral peaks. Choosing five spectral peaks centered at $\omega_1 + [0, 3\delta, 4\delta, 9\delta, 11\delta]$, 10 unique pairwise combinations are possible as indicated in Tab. 4.3.

Table 4.3: Beating frequencies resulting from pairwise combinations of five spectral peaks centered at $[\omega_1, \omega_2 = \omega_1 + 3\delta, \omega_3 = \omega_1 + 4\delta, \omega_4 = \omega_1 + 9\delta, \omega_5 = \omega_1 + 11\delta]$.

$\omega_2 - \omega_1 = 3\delta$	$\omega_3 - \omega_2 = 1\delta$	$\omega_4 - \omega_3 = 5\delta$	$\omega_5 - \omega_4 = 2\delta$
$\omega_3 - \omega_1 = 4\delta$	$\omega_4 - \omega_2 = 6\delta$	$\omega_5 - \omega_3 = 7\delta$	
$\omega_4 - \omega_1 = 9\delta$	$\omega_5 - \omega_2 = 8\delta$		
$\omega_5 - \omega_1 = 11\delta$			

As shown in Fig 4.6 and Tab. 4.3, these beating frequencies vary regularly except for the missing 10δ. This is not only a solution to the problem, but the optimal solution given that, for a set number of frequencies, n, the greatest number of unique discrete separations, $(n^2 - n)/2$, are retrieved for the smallest possible bandwidth. This solution, already used in radio science, is known as the **Golomb ruler** [88]. For $n = 2, 3$ and 4 the Golomb ruler is not only the optimal, but also a perfect solution, such that the bandwidth and number of unique separations grow equally fast with n. In Fig. 4.6, an example of the fifth Golomb ruler is presented. While this solution is still an optimal solution, due to the missing 10δ, it is no longer a perfect solution. Although no analytical model exists to find the optimal Golomb ruler, several optimal rulers all the way up to $n = 28$ have already been confirmed [89].

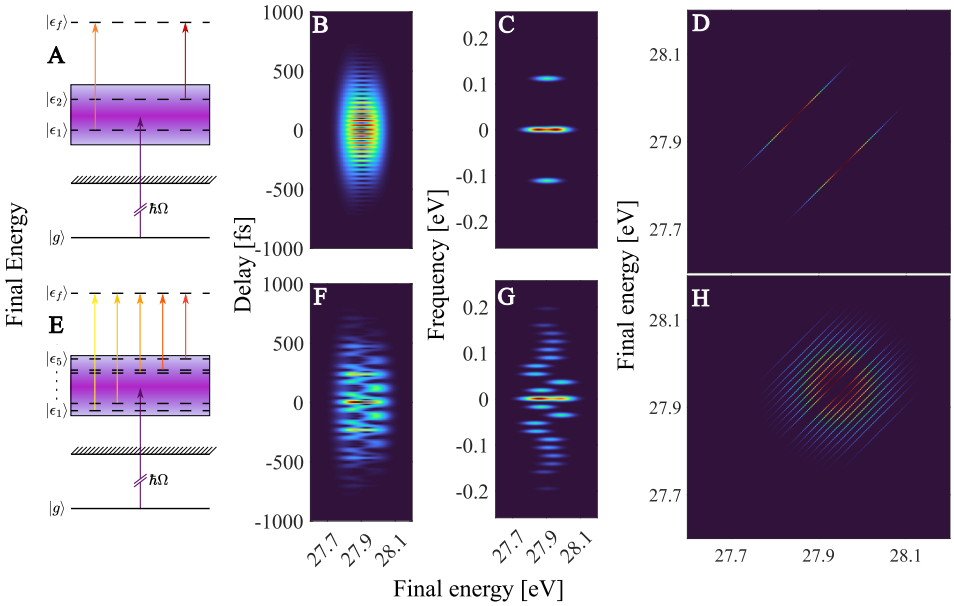

Figure 4.7: Comparison between the KRAKEN (top row) and Poly-KRAKEN (bottom row) protocols. (A,E) show energy diagrams; (B,F) spectrograms of the photoelectron spectra; (C,G) their respective Fourier transforms; and (D,H) the resulting sparse density matrices. Simulations are based on a finite pulse model [74], with all conditions held constant except the number and selection of spectral components. Note that the Golomb ruler is flipped compared to Fig. 4.6 and 4.8, resulting in the following Golomb ruler [0, 2δ, 7δ, 8δ, 11δ]. Adapted from **Paper VI**.

4.3.1 KRAKEN vs. Poly-KRAKEN

We present simulations (based on a finite pulse model [74]) of KRAKEN and Poly-KRAKEN measurements in Fig. 4.7 (see **Paper VI**). In A and E, the bi- and poly-chromatic ionization protocols are shown. The resulting spectra as a function of delay are presented in B and F respectively. The Fourier transform of these spectrograms displays the resulting signal in the frequency domain in C and G respectively. Showing that Poly-KRAKEN allows for a more efficient usage of the temporal and spectral domains simultaneously. The energy shifts, arising from differences in the central frequency of each frequency pair, must be corrected to ensure accurate alignment of the retrieved density matrix elements. Finally, the retrieved sparse density matrices are presented in D and H. It is clear that, with a well-chosen poly-chromatic field based on a Golomb ruler, Poly-KRAKEN enables a more efficient measurement, with the retrieval of 10 sub-diagonals at once.

Although Poly-KRAKEN retrieves multiple sub-diagonals simultaneously, it is not fully a single-scan protocol, as the main diagonal still requires an independent measurement, similar to KRAKEN. However, it is a faster way to obtain a large set of the photoelectron density matrix. For example, the six sub-diagonals in **Paper V** took

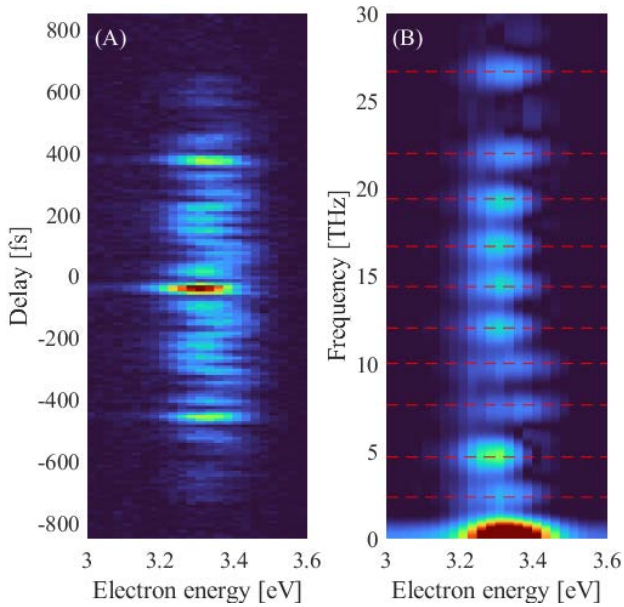

Figure 4.8: Experimental spectra as a function of delay (A) and its FFT (B) obtained in helium with Poly-KRAKEN.

about six hours of measurement time, while the ten sub-diagonals in **Paper VI** only took about two hours. In both cases, the signal strength for a given sub-diagonal should be balanced against the energy resolution since they are inversely proportional to each other. In this regard, Poly-KRAKEN is less flexible than KRAKEN, as all spectral components are generated simultaneously, limiting the ability to independently increase the strength of a pair of spectral components.

4.3.2 Experimental Poly-KRAKEN measurements

In **Paper VI**, we study the photoionization process of helium using the 17th harmonic generated in argon ($\approx$ 26.35 eV). The IR pulse is generated with a pulse energy of 4 mJ, a duration of 20 fs, and a central wavelength of 800 nm at a repetition rate of 3 kHz. The probe pulse contains multiple spectral components created using a mask described in earlier sections, resulting in components at wavelengths of $[760, 780, 787, 824, 840]$ nm, each with an approximate bandwidth of 3 nm (see Fig 4.6).

Fig. 4.8 shows (A) the measured spectra as a function of pump-probe delay and (B) their Fourier transform. The individual spectral components are clearly visible and separable in the frequency domain. This enables direct access to each component's spectral amplitude and phase. Similar to the KRAKEN protocol, each spectral ampli-

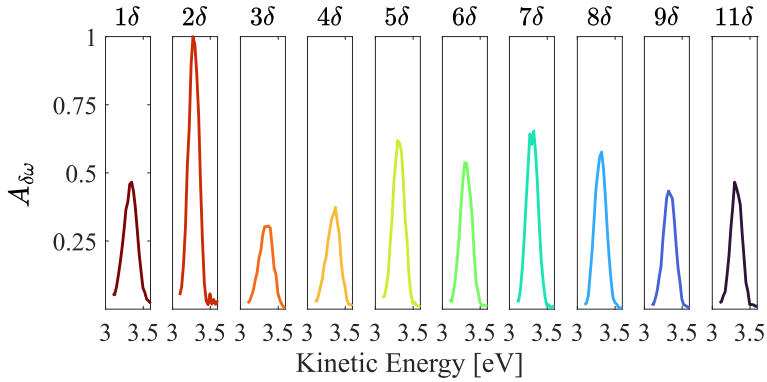

Figure 4.9: The experimentally retrieved sub-diagonal amplitudes of the density matrix obtained in helium using Poly-KRAKEN. The sub-diagonal amplitudes are normalized according to Eq. (4.5).

tude corresponds to a unique $\delta\omega$ and can be assigned to the appropriate sub-diagonal of the sparse density matrix. Each spectral component also has to be shifted depending on the specific pair of wavelengths from which it originates. Unlike the conventional KRAKEN protocol, we do not need to account for different Stark shifts between sub-diagonals, since all components are generated simultaneously in the same conditions. The main diagonal is obtained as in KRAKEN, by alternating measurements with and without a probe using a shutter.

Fig. 4.9 presents the amplitudes obtained using the Poly-KRAKEN protocol in helium. However, we do not get a decreasing slope of the amplitudes as a function of $\delta\omega$, as in Fig. 4.3.

Our first idea to explain this result was the influence of incoherent IR light, due to amplified spontaneous emission. This lead us to improve on the experimental method by measuring the coherent part of the spectrum, using the d-scan technique, based on second harmonic generation, see **Paper VII**. Since only the coherent part of the spectrum contributes to the signal, this must be accounted for in the normalization procedure according to

$$\rho_e(\epsilon_1, \epsilon_1 + \delta\omega) = \frac{A_{\delta\omega}(\epsilon_1)}{\sqrt{I^{\mathrm{coh}}_{\omega_1} q_{\omega_1} I^{\mathrm{coh}}_{\omega_2} q_{\omega_2}}}, \tag{4.15}$$

where $I^{\mathrm{coh}}_{\omega_i}$ are the coherent integrated spectral intensities and q_{ω_i} are the relative spectrometer responses at ω_1 and ω_2. Although we have observed varying degrees of coherence across the spectrum, which we could correct for, this did not explain the amplitude variation observed in 4.9.

Our second idea was to examine the influence of the frequency dependence of the CC transition matrix elements $\mu_{\epsilon_f,\epsilon_i}$. In **Papers IV** and **V**, we assumed that these transition matrix elements remain approximately constant across the spectral width of the photoelectron wave-packet. However, as discussed in the supplementary information of **Paper V**, this assumption does not necessarily hold over the full bandwidth of the IR pulse. The frequency-dependent dipole transition matrix element affects KRAKEN and Poly-KRAKEN differently. In KRAKEN, one frequency component remains fixed while the other is scanned across the IR bandwidth. Consequently, the distortion of the reconstructed density matrix varies linearly with $\delta\omega$. Depending on which end of the IR spectrum is kept fixed, the calculated purity of the density matrix may be slightly overestimated or underestimated relative to its true value. This small deviation justified treating the effect as negligible in **Paper V**.

In contrast, Poly-KRAKEN is more sensitive to this frequency dependence because it employs multiple frequency pairs simultaneously. Unlike KRAKEN, where the dependence is approximately linear, Poly-KRAKEN uses pairwise combinations based on a Golomb ruler sequence, producing a more complex interplay of matrix elements. Since the amplitude and phase of the transition matrix elements differ between angular channels, accurately correcting for these effects in the experimental data remains difficult. At the time this thesis is being written, we are investigating different ways to account for these effects, both experimentally and theoretically. More details can be found in **Paper VI**.

Improvements such as using the coherent IR spectra for normalization and retrieving ten sub-diagonals in a single measurement represent a major step forward. Despite remaining challenges, such as accounting for the frequency dependence of CC transition matrix elements, Poly-KRAKEN represents a powerful and efficient new tool for multidimensional QST, offering faster and more comprehensive access to the photoelectron density matrix than previously possible.

Chapter 5

Summary & outlook

5.1 Summary

In this thesis, we have presented a new experimental setup that enables attosecond photoelectron metrology with a stability and flexibility previously unattainable. By implementing an active temporal stabilization scheme, we achieved a temporal jitter below 13 as (RMS) over several hours. This enables high-precision experiments combining an XUV APT pump and an IR probe, measured with a photoelectron spectrometer achieving a spectral-resolution better than 80 meV for electrons with a kinetic energy below 5 eV.

The capabilities of the setup were demonstrated through two RABBIT measurements of resonant photoionization. In helium, two-photon ionization via the 3p, 4p, and 5p Rydberg states was studied using angular-resolved and angular-integrated photoelectron detection. The addition of a polarizer in the IR probe allowed us to perform RABBIT measurements with cross-polarized pump and probe, making it possible to isolate one angular channel, while maintaining high spectral-resolution. In argon, we studied photoionization across the $3s^{-1}4p$ Fano resonance. Our high spectral-resolution was essential to resolve the SO splitting (177 meV), and the possibility to spectrally shape the probe pulse allowed us to observe bandwidth-dependent phase variations resulting from interactions in the final state.

Finally, we proposed and demonstrated a novel quantum measurement protocol, KRA-KEN, for reconstructing the density matrix of a photoelectron wave-packet. This extends attosecond metrology beyond the limits of conventional wave-based protocols like RABBIT. Our experimental results show good agreement with theoretical predictions, establishing KRAKEN as a reliable tool for measuring the quantum state of

the photoelectron created by the ionization of a neutral atom. An extension of the protocol, Poly-KRAKEN, using spectral Golomb rulers, is also presented.

These developments mark a significant step forward in our ability to probe and manipulate ultrafast quantum processes, paving the way for new forms of control over electron dynamics on their natural timescale.

5.2 Outlook

The upgraded setup now enables ultra-stable, long-duration measurements with improved signal-to-noise ratios and the ability to resolve slow temporal modulations through longer delay scans. A coming upgrade to a new acquisition card is expected to double the spectral-resolution, paving the way for narrow-band RABBIT experiments in molecular systems such as N_2 and H_2, allowing us to resolve dynamics previously inaccessible. The improved resolution would also greatly benefit us in successfully performing a KRAKEN measurement in resonant photoionization systems, such as in the presence of a Fano resonance theoretically covered in **Paper IV**.

In **Paper IV**, we also proposed theoretically a "quantum control" experiment based on tuning the spectral width of the XUV pulse to manipulate the overlap between SO-split states (see Fig. 5.1) and therefore the entanglement. Previously, the long acquisition time required for each data point (approximately 8 hours) made this measurement impossible in practice. However, the introduction of the Poly-KRAKEN protocol now makes such measurements experimentally feasible.

Another promising direction is Rainbow KRAKEN [90], a spectrally resolved extension of the KRAKEN method. This protocol introduces a narrowband IR spectral reference locked to the XUV pulse, and uses a spectrally broad probe pulse. The introduction of a fixed reference moves the signal away from the zero-frequency region in the frequency domain, thereby removing low-frequency noise from the signal. This enables continuous access to the density matrix elements across the probe bandwidth within a single scan. The current setup does not yet support this method, but with some adjustments to the pump beam line it may soon be possible to assess its experimental feasibility.

We also aim to implement a *multi-pass cell* [91, 92] to broaden the spectral bandwidth of both interferometer arms, enabling access to density matrix elements further from the main diagonal. Furthermore, by frequency doubling the laser and replacing the interferometer's beam splitter with a dichromatic one, sending ω to the probe arm and 2ω to the pump arm. In such a configuration, emission and absorption paths from neighboring harmonics can be distinguished (see Fig. 5.2) and studied separately, as

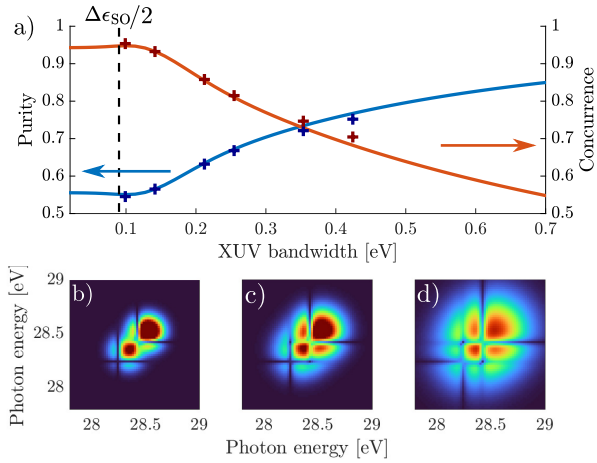

Figure 5.1: (a) Purity (blue) and concurrence (red) $C = \sqrt{2[1 - Tr(\rho_e^2)]}$, calculated directly as a function of XUV bandwidth. Blue and red crosses represent the corresponding quantities extracted via the KRAKEN protocol. The vertical dashed line indicates half the SO splitting energy ($\Delta\epsilon_{SO}$). Bandwidths smaller than $\Delta\epsilon_{SO}/2$, fully spectrally resolve the SO-split ionic states. (b–d) Absolute value of the photoelectron density matrix $|\rho_e(\epsilon_1, \epsilon_1 + \delta\omega)|$ shown for XUV bandwidths of $\delta\Omega$ = 0.14 eV (b), 0.21 eV (c), and 0.35 eV (d). Adapted from **Paper IV**.

the probe frequency is much smaller than the difference frequency between two consecutive harmonics. This would thereby allow for the simultaneous retrieval of density matrix elements from multiple, spectrally distinct photoelectron wave-packets.

In parallel with further investigation of photoionization processes, future work could also open other areas within quantum attosecond science. For example, we could explore generating and characterizing quantum XUV light [93, 94] or using as a probe quantum IR light [95]. Performing Poly-KRAKEN measurements with non-classical light would open fundamentally new regimes of light-matter interaction, where coherence and entanglement properties are governed not only by the atomic system but also by the quantum state of the light field itself.

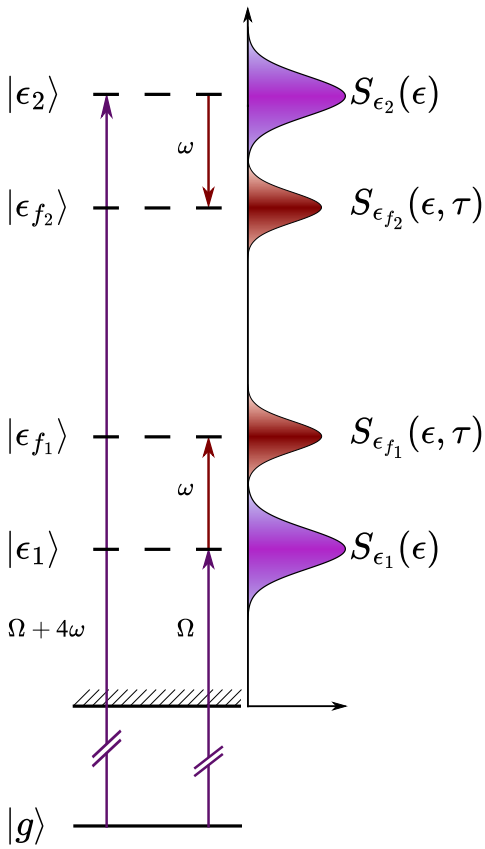

Figure 5.2: Photoionization due to harmonics with frequencies Ω and $\Omega + 4\omega$, in the presence of a probe with frequency ω. Resulting in spectrally resolved emission and absorption paths.

References

[1] A. Einstein. Über einen die erzeugung und verwandlung des lichtes betreffenden heuristishen gesichtspunk. *Annalen der Physik*, 332:132–148, 1905.

[2] H. Hertz. Ueber einen einfluss des ultravioletten lichtes auf die electrische entladung. *Ann. Phys.*, 267:pp 983–1000, 1887.

[3] K. Siegbahn and K. Edvarson. β-ray spectroscopy in the precision range of 1:105. *Nuclear Physics*, 1(8):137–159, 1956.

[4] T. Mainman. Stimulated optical radiation in ruby. *Nature*, 187:pp. 493–494, 1960.

[5] F. J. McClung and R. W. Hellwarth. Giant optical pulsations from ruby. *Appl. Opt.*, 1(S1):103–105, 1962.

[6] L. E. Hargrove, R. L. Fork, and M. A. Pollack. Locking of he–ne laser modes induced by synchronous intracavity modulation. *Applied Physics Letters*, 5(1):4–5, 1964.

[7] D. E. Spence, P. N. Kean, and W. Sibbett. 60-fsec pulse generation from a self-mode-locked ti:sapphire laser. *Opt. Lett.*, 16(1):42–44, 1991.

[8] A. J. DeMaria, D. A. Sttser, and H. Heynau. Self mode□locking of lasers with saturable absorbers. *Appl. Phys. Lett.*, 7(8), 1966.

[9] C. V. Shank and E. P. Ippen. Subpicosecond kilowatt pulses from a mode-locked cw dye laser. *Appl. Phys. Lett.*, 24(8), 1974.

[10] A. H. Zewail. Laser femtochemistry. *Science*, 242(4886):1645–1653, 1988.

[11] D. Strickland and G. Mourou. Compression of amplified chirped optical pulses. *Optics Communications*, 55(6):447–449, 1985.

[12] M. Ferray, A. L'Huillier, L. A. Lompre, G. Mainfray, and C. Manus. Multiple-harmonic converion of 1064 nm radiation in rare gases. *J. Phys. B: At. Mol. Opt. Phys.*, 21(L31), 1988.

[13] P. M. Paul, E. S. Toma, P. Breger, G. Mullot, F. Auge, P. Balcou, H. G. Muller, and P. Agostini. Observation of a train of attosecond pulses from high harmonic generation. *Science*, 292:1689–1692, 2001.

[14] J. Itatani, F. Quéré, G. L. Yudin, M. Y. Ivanov, F. Krausz, and P. B. Corkum. Attosecond streak camera. *Phys. Rev. Lett.*, 88:173903, 2002.

[15] K. Klünder, J. M. Dahlström, M. Gisselbrecht, T. Fordell, M. Swoboda, D. Guénot, P. Johnsson, J. Caillat, J. Mauritsson, A. Maquet, R. Taïeb, and A. L'Huillier. Probing single-photon ionization on the attosecond time scale. *Phys. Rev. Lett.*, 106:143002, 2011.

[16] E. P. Månsson, D. Guénot, C. L. Arnold, D. Kroon, S. Kasper, J. M. Dahlström, E. Lindroth, A. S. Kheifets, A. L'Huillier, S. L. Sorensen, and M. Gisselbrecht. Double ionization probed on the attosecond timescale. *Nature Physics*, 10:207–211, 2014.

[17] S. Heuser, A. Jiménez Galán, C. Cirelli, C. Marante, M. Sabbar, R. Boge, M. Lucchini, L. Gallmann, I. Ivanov, A. S. Kheifets, J. M. Dahlström, E. Lindroth, L. Argenti, F. Martín, and U. Keller. Angular dependence of photoemission time delay in helium. *Phys. Rev. A*, 94:063409, 2016.

[18] M. Huppert, I. Jordan, D. Baykusheva, A. von Conta, and H. J. Wörner. Attosecond delays in molecular photoionization. *Phys. Rev. Lett.*, 117:093001, 2016.

[19] S. Nandi, E. Plésiat, S. Zhong, A. Palacios, D. Busto, M. Isinger, L. Neoričić, C. L. Arnold, R. J. Squibb, R. Feifel, P. Decleva, A. L'Huillier, F. Martín, and M. Gisselbrecht. Attosecond timing of electron emission from a molecular shape resonance. *Science Advances*, 6(31):eaba7762, 2020.

[20] R. Locher, L. Castiglioni, M. Lucchini, M. Greif, L. Gallmann, J. Osterwalder, M. Hengsberger, and U. Keller. Energy-dependent photoemission delays from noble metal surfaces by attosecond interferometry. *Optica*, 2(5):405–410, 2015.

[21] L. Kasmi, M. Lucchini, L. Castiglioni, P. Kliuiev, J. Osterwalder, M. Hengsberger, L. Gallmann, P. Krüger, and U. Keller. Effective mass effect in attosecond electron transport. *Optica*, 4(12):1492–1497, 2017.

[22] M. Swoboda, T. Fordell, K. Klünder, J. M. Dahlström, M. Miranda, C. Buth, K. J. Schafer, J. Mauritsson, A. L'Huillier, and M. Gisselbrecht. Phase measurement of resonant two-photon ionization in helium. *Phys. Rev. Lett.*, 104:103003, 2010.

[23] L. Drescher, T. Witting, O. Kornilov, and M. J. J. Vrakking. Phase dependence of resonant and antiresonant two-photon excitations. *Phys. Rev. A*, 105:L011101, 2022.

[24] M. Kotur, D. Guénot, D. Jiménez-Galán, Á.and Kroon, E. W. Larsen, M. Louisy, S. Bengtsson, M. Miranda, J. Mauritsson, C. L. Arnold, S. E. Canton, M. Gisselbrecht, T. Carette, J. M. Dahlström, E. Lindroth, A. Maquet, L. Argenti, F. Martín, and A. L'Huillier. Spectral phase measurement of a fano resonance using tunable attosecond pulses. *Nature communications*, 7(10566), 2016.

[25] V. Gruson, L. Barreau, ⊠. Jiménez-Galan, F. Risoud, J. Caillat, A. Maquet, B. Carré, F. Lepetit, J. F. Hergott, T. Ruchon, L. Argenti, R. Taïeb, F. Martín, and P. Salières. Attosecond dynamics through a fano resonance: Monitoring the birth of a photoelectron. *Science*, 354:734–738, 2016.

[26] S. Haessler, B. Fabre, J. Higuet, J. Caillat, T. Ruchon, P. Breger, B. Carré, E. Constant, A. Maquet, E. Mével, P. Salières, R. Taïeb, and Y. Mairesse. Phase-resolved attosecond near-threshold photoionization of molecular nitrogen. *Phys. Rev. A*, 80:011404, 2009.

[27] D. Akoury, K. Kreidi, T. Jahnke, T. Weber, A. Staudte, M. Schöffler, N. Neumann, J. Titze, L. P. H. Schmidt, A. Czasch, O. Jagutzki, R. A. Costa Fraga, R. E. Grisenti, R. Díez Muiño, N. A. Cherepkov, S. K. Semenov, P. Ranitovic, C. L. Cocke, T. Osipov, H. Adaniya, J. C. Thompson, M. H. Prior, A. Belkacem, A. L. Landers, H. Schmidt-Böcking, and R. Dörner. The simplest double slit: Interference and entanglement in double photoionization of h₂. *Science*, 318(5852):949–952, 2007.

[28] M. C. Tichy, F. Mintert, and A. Buchleitner. Essential entanglement for atomic and molecular physics. *J. Phys. B: At. Mol. Opt. Phys.*, 44(19):192001, 2011.

[29] S. Pabst, L. Greenman, P. J. Ho, D. A. Mazziotti, and R. Santra. Decoherence in attosecond photoionization. *Phys. Rev. Lett.*, 106:053003, 2011.

[30] S. Carlström, J. Mauritsson, K. J. Schafer, A. L'Huillier, and M. Gisselbrecht. Quantum coherence in photo-ionisation with tailored xuv pulses. *Phys. Rev. Lett.*, 106:053003, 2011.

[31] T. Nishi, E. Lötstedt, and K. Yamanouchi. Entanglement and coherence in photoionization of h_2 by an ultrashort xuv laser pulse. *Phys. Rev. A*, 100:013421, 2019.

[32] M. J. J. Vrakking. Control of attosecond entanglement and coherence. *Phys. Rev. Lett.*, 126:113203, 2021.

[33] D. Busto, L. Barreau, M. Isinger, C. Alexandridi, A. Hart, S. Zhong, R. J. Squibb, D. Kroon, and S. Plogmaker. Time-frequency representation of autoionization dunamics in helium. *J. Phys. B: At. Mol. Opt. Phys.*, 51(4):044002, 2018.

[34] L. Koll, L. Maikowski, L. Drescher, T. Witting, and M. J. J. Vrakking. Experimental control of quantum-mechanical entanglement in an attosecond pump-probe experiment. *Phys. Rev. Lett.*, 128:043201, 2022.

[35] C. Bourassin-Bouchet, L. Barreau, V. Gruson, J.-F. Hergott, F. Quéré, P. Salières, and T. Ruchon. Quantifying decoherence in attosecond metrology. *Phys. Rev. X*, 10:031048, 2020.

[36] P. F. Moulton. Spectroscopic and laser characteristics of ti:al203. *J. Opt. Soc. Am. B*, 3(1):125–133, 1986.

[37] J. Hecht. Short history of laser development. *Optical Engineering*, 49(9):091002, 2010.

[38] G. Cheriaux, P. Rousseau, F. Salin, J. P. Chambaret, B. Walker, and L. F. Dimauro. Aberration-free stretcher design for ultrashort-pulse amplification. *Opt. Lett.*, 21(6):414–416, 1996.

[39] P. Tournois. Acousto-optic programmable dispersive filter for adaptive compensation of group delay time dispersion in laser systems. *Optics Communications*, 140(4):245–249, 1997.

[40] T. Oksenhendler, D. Kaplan, P. Tournois, G. M. Greetham, and F. Estable. Intracavity acousto-optic programmable gain control for ultra-wide-band regenerative amplifiers. *Appl. Phys. B.*, 83:491–494, 2006.

[41] S. Backus, C. G. Durfee, G. Mourou, H. C. Kapteyn, and M. M. Murnane. 0.2-tw laser system at 1 khz. *Opt. Lett.*, 22(16):1256–1258, 1997.

[42] E. Treacy. Optical pulse compression with diffraction gratings. *IEEE Journal of Quantum Electronics*, 5(9):454–458, 1969.

[43] A. Moulet, A. Grabielle, C. Cornaggia, N. Forget, and T. Oksenhendler. Single-shot, high-dynamic-range measurement of sub-15 fs pulses by self-referenced spectral interferometry. *Opt. Lett.*, 35(22):3856–3858, 2010.

[44] T. Oksenhendler, S. Coudreau, and N. Forget. Self-referenced spectral interferometry. *Appl. Phys. B.*, 99:7–12, 2010.

[45] P. A. Franken, A. E. Hill, C. W. Peters, and G. Weinreich. Generation of optical harmonics. *Phys. Rev. Lett.*, 7:118–119, 1961.

[46] A. McPherson, G. Gibson, H. Jara, U. Johann, T. S. Luk, I. A. McIntyre, K. Boyer, and C. K. Rhodes. Studies of multiphoton production of vacuum-ultraviolet radiation in the rare gases. *J. Opt. Soc. Am. B*, 4(4):595–601, 1987.

[47] M. Sayrac, A. A. Kolomenskii, and H. A. Schuessler. Pressure optimization and phase matching of high harmonics generation in co2 and c2h2 molecular gases. *Journal of Electron Spectroscopy and Related Phenomena*, 229:1–6, 2018.

[48] S. Ghimire, A. D. DiChiara, E. Sistrunk, P. Agostini, L. F. DiMauro, and D. A. Reis. Observation of high-order harmonic generation in a bulk crystal. *Nature Phys*, 7:138–141, 2011.

[49] T. T. Luu, Z. Yin, A. Jain, T. Gaumnitz, Y. Pertot, J. Ma, and H. J. Wörner. Extreme–ultraviolet high–harmonic generation in liquids. *Nat. Commun.*, 9(3723), 2018.

[50] P. B. Corkum. Plasma perspective on strong field multiphoton ionization. *Phys. Rev. Lett.*, 71:1994–1997, 1993.

[51] K. C. Kulander, K. J. Schafer, and J. L. Krause. *Dynamics of Short-Pulse Excitation, Ionization and Harmonic Conversion*, pages 95–110. Springer US, Boston, MA, 1993.

[52] M. Lewenstein, P. Balcou, M. Y. Ivanov, A. L'Huillier, and P. B. Corkum. Theory of high-harmonic generation by low-frequency laser fields. *Phys. Rev. A*, 49:2117–2132, 1994.

[53] S. Bengtsson, E. Simpson, N. Ibrakovic, S. Ek, A. Olofsson, T. Causer, and J. Mauritsson. Experimental observation of longer trajectories than previously observed in high-order harmonic generation. *Physical Review A*, 108, 2023.

[54] A. S. Johnson, T. Avni, E. W. Larsen, D. R. Austin, and J. P. Marangos. Attosecond soft x-ray high harmonic generation. *Philos Trans A Math Phys Eng Sci.*, 377, 2019.

[55] C. M. Heyl, C. L. Arnold, A. Couairon, and A. L'Huillier. Introduction to macroscopic power scaling principles for high-order harmonic generation. *Journal of Physics B: Atomic, Molecular and Optical Physics*, 50(1):013001, 2016.

[56] M. Bellini, C. Lyngå, A. Tozzi, M. B. Gaarde, T. W. Hänsch, A. L'Huillier, and C.-G. Wahlström. Temporal coherence of ultrashort high-order harmonic pulses. *Phys. Rev. Lett.*, 81:297–300, 1998.

[57] C.-G. Wahlström, J. Larsson, A. Persson, T. Starczewski, S. Svanberg, P. Salières, P. Balcou, and A. L'Huillier. High-order harmonic generation in rare gases with an intense short-pulse laser. *Phys. Rev. A*, 48:4709–4720, 1993.

[58] M. Hentschel, R. Kienberger, C. Spielmann, G. A. Reider, N. Milosevic, T. Brabec, P. Corkum, U. Heinzmann, M. Drescher, and F. Krausz. Attosecond metrology. *Nature*, 414:509–513, 2001.

[59] K. Varjú, Y. Mairesse, B. Carré, M. B. Gaarde, P. Johnsson, S. Kazamias, R. López-Martens, J. Mauritsson, K. J. Schafer, P. Balcou, A. L'huillier, and P. Salières. Frequency chirp of harmonic and attosecond pulses. *Journal of Modern Optics*, 52(2-3):379–394, 2005.

[60] C. Guo, A. Harth, S. Carlström, Y. Cheng, S. Mikaelsson, E. Mårsell, C. Heyl, M. Miranda, M. Gisselbrecht, M. B. Gaarde, K. J. Schafer, A. Mikkelsen, J. Mauritsson, C. L. Arnold, and A. L'Huillier. Phase control of attosecond pulses in a train. *Journal of Physics B: Atomic, Molecular and Optical Physics*, 51(3):034006, 2018.

[61] M. Isinger, D. Busto, S. Mikaelsson, S. Zhong, C. Guo, P. Salieres, C. Arnold, A. L'Huillier, and M. Gisselbrecht. Accuracy and precision of the rabbit technique. *Phil. Trans. R. Soc. A.*, 377, 2019.

[62] D. Kroon. *Attosecond interferometry: techniques and spectroscopy*. PhD thesis, Lund University, 2016.

[63] M. Miranda, T. Fordell, C. L. Arnold, A. L'Huillier, and H. Crespo. Simultaneous compression and characterization of ultrashort laser pulses using chirped mirrors and glass wedges. *Opt. Express*, 20(1):688–697, 2012.

[64] M. Miranda, A. C. L., T. Fordell, F. Silva, B. Alonso, R. Weigand, A. L'Huillier, and H. Crespo. Characterization of broadband few-cycle laser pulses with the d-scan technique. *Opt. Express*, 20(17):18732–18743, 2012.

[65] J. L. Wiza. Microchannel plate detectors. *Nuclear Instruments and Methods*, 162(1):587–601, 1979.

[66] M. Sabbar, S. Heuser, R. Boge, M. Lucchini, L. Gallmann, C. Cirelli, and U. Keller. Combining attosecond xuv pulses with coincidence spectroscopy. *Rev. Sci. Instrum.*, 10(85):103113, 2014.

[67] A. T. J. B. Eppink and D. H. Parker. Velocity map imaging of ions and electrons using electrostatic lenses: Application in photoelectron and photofragment ion imaging of molecular oxygen. *Review of Scientific Instruments*, 68(9):pp. 3477–3484, 1997.

[68] W. H. Richardson. Bayesian-based iterative method of image restoration. *J. Opt. Soc. A*, 62(1):pp 55–59, 1972.

[69] L. B. Lucy. An iterative technique for the rectification of observed distributions. *Astron. J.*, 79(745), 1974.

[70] G. A. Garcia, L. Nahon, and I. Powis. Two-dimensional charged particle image inversion using a polar basis function expansion. *Rev. Sci. Instrum.*, 11(75):pp 4989–4996, 2004.

[71] U. Becker. Photoelectron spectroscopy of atoms. *Journal of Electron Spectroscopy and Related Phenomena*, 75:23–34, 1995.

[72] J. M. Dahlström and E. Lindroth. Study of attosecond delays using perturbation diagrams and exterior complex scaling. *J. Phys. B: At. Mol. Opt. Phys*, 47, 2014.

[73] A. Jiménez-Galán, L. Argenti, and F. Martín. Modulation of attosecond beating in resonant two-photon ionization. *Phys. Rev. Lett.*, 113:263001, 2014.

[74] F. Jiménez-Galán, Á.and Martín and L. Argenti. Two-photon finite-pulse model for resonant transitions in attosecond experiments. *Phys. Rev. A*, 93:023429, 2016.

[75] U. Fano. Effects of configuration interaction on intensities and phase shifts. *Phys. Rev.*, 124:1866–1878, 1961.

[76] V. Véniard, R. Taïeb, and A. Maquet. Phase dependence of (n+1)-color (n>1) ir-uv photoionization of atoms with higher harmonics. *Phys. Rev. A*, 54:721–728, 1996.

[77] C. Bourassin-Bouchet and M. E. Couprie. Partially coherent ultrafast spectrography. *Nat. Commun.*, 6, 2015.

[78] M. Turconi, L. Barreau, D. Busto, M. Isinger, C. Alexandridi, A. Harth, R. J. Squibb, D. Kroon, C. L. Arnold, R. Feifel, M. Gisselbrecht, L. Argenti, F. Martín, A. L'Huillier, and P. Salières. Spin–orbit-resolved spectral phase measurements around a fano resonance. *Journal of Physics B: Atomic, Molecular and Optical Physics*, 53(18):184003, 2020.

[79] M. Mendoza, P. A. Schulz, R. O. Vallejos, and C. H. Lewenkopf. Fano resonances in the conductance of quantum dots with mixed dynamics. *Phys. Rev. B*, 77:155307, 2008.

[80] A. Autuori, D. Platzer, M. Lejman, G. Gallician, L. Maëder, A. Covolo, L. Bosse, M. Dalui, D. Bresteau, J. Hergott, O. Tcherbakoff, H. J. B. Marroux, V. Loriot, F. Lépine, L. Poisson, R. Taïeb, J. Caillat, and P. Salières. Anisotropic dynamics of two-photon ionization: An attosecond movie of photoemission. *Science Advances*, 8(12):eabl7594, 2022.

[81] J. Vinbladh, J. M. Dahlström, and E. Lindroth. Many-body calculations of two-photon, two-color matrix elements for attosecond delays. *Phys. Rev. A*, 100:043424, 2019.

[82] B. Bertlmann and N. Friis. *Modern Quantum Theory: From Quantum Mechanics to Entanglement and Quantum Information*. Oxford Academic, 2023.

[83] J. J. Sakurai and J. Napolitano. *Modern Quantum Mechanics, 3rd Ed.* Cambridge University Press, 2021.

[84] M. D. Hoffman and A. Gelman. The no-u-turn sampler: Adaptively setting path lengths in hamiltonian monte carlo. *J. Mach. Learn. Res.*, 15:1593–1623, 2014.

[85] J. Vinbladh, J. M. Dahlström, and E. Lindroth. Relativistic two-photon matrix elements for attosecond delays. *Atoms*, 10(3), 2022.

[86] A. Bushleitner, c. Viviescas, and M. Tiersch. *Entaglement and Decoherence: Foundations and Modern Trends, Lect. Notes Phys. 768*. Springer, Berlin Heidelberg, 2009.

[87] R. D. Cowen. *The Theory of Atomic Structure and Spectra*. University of California press, 1981.

[88] W. C. Babcock. Intermodulation interference in radio systems. In *Bell System Technical Journal, 32(1)*, 1953.

[89] distributed.net, *Completion of OGR-28 project*, Retrieved 2024-03-35.

[90] H. Laurell, J. Baños-Gutiérrez, A. L'Huillier, B. D., and D. Finkelstein-Shapiro. A multidimensional approach to quantum state tomography of photoelectron wavepackets. *Sci. Rep.*, 15, 2025.

[91] L. Daniault, J. Kaur, G. Gallé, C. Sire, F. Sylla, and R. Lopez-Martens. Sub-2-cycle post-compression of multi-mj energy ti:sapphire laser pulses in a gas-filled multi-pass cell. *Opt. Lett.*, 49(23):6833–6836, 2024.

[92] A. Viotti, M. Seidel, E. Escoto, E. Rajhans, W. P. Leemans, I. Hartl, and C. M. Heyl. Multi-pass cells for post-compression of ultrashort laser pulses. *Optica*, 9(2):197–216, 2022.

[93] D. Theidel, V. Cotte, R. Sondenheimer, V. Shiriaeva, M. Froidevaux, V. Severin, P. Model, A. Merdji-Larue, S. Fröhlich, K. Weber, U. Morgner, M. Kovacev, J. Biegert, and H. Merdji. Evidence of the quantum-optical nature of high-harmonic generation. *arXiv:2405.15022*, 2024.

[94] M. E. Tzur, N. Mor, C. Yaffe, M. Birk, A. Rasputnyi, O. Kneller, I. Nisim, I. Kaminer, M. Krüger, N. Dudovich, and O. Cohen. Measuring and controlling the birth of quantum attosecond pulses. *arXiv:2502.09427*, 2025.

[95] J. Heimerl, A. Mikhaylov, S. Meier, H. Höllerer, I. Kaminer, M. Chekhova, and P. Hommelhoff. Multiphoton electron emission with non-classical light. *Nat. Phys.*, 20:945–950, 2024.

Acknowledgments

During the past five years, I have worked with attosecond physics in our lab, first as a Master's student, then as a lab assistant, and finally as a PhD student. These years have been some of the most exciting, interesting, and challenging of my life, and none of it would have been possible without the support of many incredible people.

First and foremost, I would like to thank my main supervisor, Anne L'Huillier. You first introduced me to attosecond physics in a course then known as Light-Matter Interaction. From that course, two things became clear instantly: I knew the field I wanted to pursue for my PhD, and, like many before and after me, I was deeply impressed by your humble nature and your remarkable ability to teach even the most complex topics as if they were just a gentle hill we climbed together. Thank you for believing in me and supporting me from that day forward.

I am also deeply grateful to my other supervisors, Cord Arnold, Mathieu Gisselbrecht, and David Busto. Thank you, Cord, for your great sense of humor and for guiding me through my Master's thesis during the Covid pandemic. While we may no longer be fixing lasers together, those moments will always stay with me. Thank you, Mathieu, for helping bridge the fields of attosecond and quantum physics through our many seminars and discussions. And thank you David, for being an invaluable office-mate at the start of my PhD. Your attention to detail not only helped me correct my misconceptions, but taught me that, truly, the devil lies in the details.

I would also like to thank the people from the KHz lab. Thank you Robin Weissenbilder for the countless hours spent both inside and outside the laboratory walls and the amount interesting discussions that follows. Thank you Hugo Laurell for showing me that it's absolutely fine to sing while aligning the lasers (with varying degrees of success!). Thank you Lana Neoričić for making me feel at home in a place that became the center of my life for five years. Thank you Sizuo Luo for being my friend and believing in me, even when I did not possess the ability to do so myself. As I will always have a home in China with you, you will always have one here in Sweden with me. Thank you Edoardo Boati for bringing a much needed and great new

energy to our division, for making me feel like a good person again and for introducing me to all the important people of tennis. Thank you Gustav Arvidsson for your endless supply of joy, your playful endeavors with Edoardo and telling the truth even when no one believes you. I would like to thank Christoph Dittel for filling many early mornings and late nights with meaningful conversations about things outside of work every now and then. Thank you Vénus Poulain for your unwavering support, laughter, and late nights in the lab with me and Sizuo. Thank you Saga Westerberg for all our time spent studying, aligning, and talking on the way home from work. While many, those moments were not nearly as many as I wished. Lastly I would also like to thank Samuel Eklund, Hugo Söderberg, Maxence Barre, Ron Demaja and Viktoriia Shiriaeva for the time I shared with you all.

I would also like to thank all the collaborators of the projects I have been involved with. Thank you Shiyang Zhong and David Kroon for your contribution to the new attolab setup. Thank you Fernando Martín, Roger Bello Romero, Luca Argenti, Carlos Marante, Eva Lindroth, Leon Petersson, Anton Ljungdahl, Daniel Finkelstein-Shapiro, Andreas Buchleitner, Tönu Pullerits, Shahnawaz Achmed, Anton Frisk Kock -um, Camille Lévêque, Shiriaeva Dubois, Richard Taïb and Jérémie Caillat for fruitful discussions highlighting the importance of collaborations between experiments and theory in complex atomic and quantum systems. Thank you Raimund Feifel, and especially Richard Squibb for all the help with the MBES. Thank you Jasper Peschel, Hampus Wikmark, Jan Lahl, Sylvain Maclot and Per Eng-Johnsson for the helping me further understand resonant atomic physics experimentally. Thank you Mingxuan Li and Huiyong Wang for solving countless experimental problems with us during the Poly-KRAKEN campaign, perhaps my favorite campaign. I would also like to thank Daniel Díaz Rivas, Ivan Sytcevic, Miguel Canhota, Miguel Miranda and Anne-Lise Viotti for helping me understand laser characterization and the d-scan method better. Thank you Marius for helping me start to update the gas supply lines, even if little has happened without your help since. Thank you Anka for always joining me in the coffee room to discuss some more or less crazy ideas over the years. And finally, a special thanks to Chen Guo, whom have taught me more than I can remember about lasers, optics, 'parenthood' and jokes of varying quality.

This PhD would not have been possible without the funding provided by the Wallenberg Centre for Quantum Technology (WACQT). Thank you for supporting my entire PhD and for bringing together a fantastic community of scientists and friends. Thank you Armin, Abhilash, Daniel, Hilma, Natalia, Nathaniel, Nicola, Simon, Gabriele, Max, Juan-Carlos, Claudia, Drilon and Linda for making the WACQT excursions and meetings a highlight of my PhD. Through you all, I've learned so much about quantum physics, and I've made memories for a lifetime.

I would also like to extend my thanks to all of my other attosecond colleagues. Thank

you Melvin, Yuman and Gaspard from the D-Lab. Thank you Nedjma, Praveen and Caroline from the MHz. Thank you Elisa from the 10 Hz. The community within the atto group was fundamental to my choice of doing a PhD here with you all, and will remain one of the things I'm the most grateful for during the PhD.

Of course people outside of the atto group should be thanked as well. Thank you Claes-Göran Wahlström, Lars Rippe and Charlotte Landin for all projects related to education and board meeting we have shared. Thank you Isa, Cornelia, David G., Marcus, Erik L., Johannes for making every lunch and spontaneous hallway conversation filled with laughter. I also want to thank former colleagues, whom shall not be forgotten. Thank you Emma, Samuel B., Stafanos, Alexander and Jasper for the (all too short) time we had together.

Internationally, I've been lucky to make friends through the attosecond community. Thank you Ben, Anne, Slava, Laura, Federico, Felipe, Barbara and Lisa for all the adventures and rich discussions we have shared. Knowing I have friends like you around the world fills me with joy and hope. Thank you Esa Paju for your help repairing our vacuum chamber and for the expertise that came with it. Thank you Noelle Walsh for lending us the acquisition card. Thank you Håkan Ivansson for all the help with the multitude of mask designs for our setup. And finally, thank you Alexander Brash for helping me fix the "unfixable" oscillator that haunted the second year of my PhD and for your whiskey recommendations.

Of course, none of this would function without the essential support from the administrative staff. Thank you Jörgen Larsson, Desiree Lindqvist, Anne Petersson-Jungbeck, Maria Algotsson, Åke Johansson, Anders Persson And Emelie Nihlén. And thank you to anyone not mentioned here, but who has been a part of this journey. This book would be twice as long if I were to do right by you all.

While this section is not short of friends, more than anyone else, must I also thank those who helped shape my life long before this PhD. Thank you Johan, Nathalie, Christian, Cecilia, Sonny, Veronica, Christoffer, Pontus, Jovan (Sparkles), Robert (Robban), Jennika, Ricardo, Sara, Elin, Olivia, Joakim (Jocke), Ludvig, Lea, Henrik (Berra), Jonas, Linnéa, Claudia, Natali, Michael (Mickey), Daniel (Danne), Linnéa och Kent. Thank you for all the hours we've shared. My only regret is the hours we didn't. If I have but one superpower, it must be the ability to find great people like you all and get the honor to call them my friends.

To my family, thank you for your endless support throughout every endeavor. Without you, life would feel meaningless. To my three sisters, thank you Linda, Sandra and Lotta and their husbands Markus, Sebastian and Lars. To my extended family, thank you Anders, Aston, Amos, Herman, Titti and Roger. To all my amazing nephews and nieces, thank you Hilma, Moa, Vilgot, My, Agnes, August and Henry. To the people

that left us all to early, thank you Ivar, Inga, Barbro and Tage and especially my late father Kent, who first sparked my interest in physics.

A great deal of gratitude is aimed towards my mother Lena and my father Mats. The very fact that I've made it this far is because I have always been able to rest on your shoulders when needed to. Thank you for being my parents, my friends and more than anything, for all the time we've spent together. I am no more than what you have given me the possibility to become, and my only aim as a father and a person is to follow in your footsteps.

Lastly, I would like to thank Vissla for the much needed change of scenery during our walks. Even more do I thank you Anna. You are the pillar that guides me forward and shields me when storms arrive. No words of gratitude will ever suffice to express the depth of what you mean to me, but I will spend the rest of my life trying. Thank you for giving me our son, whose light now shines at the top of this very pillar. Thank you, Love, for your smile and joy, reminding me every day of the true importance of time spent with loved ones. In your presence, Anna, Vissla and Love, only the best parts of life remain.

Author contributions

Paper I: Ultra-stable and versatile high-energy resolution setup for attosecond photoelectron spectroscopy

In this paper, we present an ultra-stable and versatile interferometer for high-energy resolution attosecond pump-probe photoelectron spectroscopy. By actively stabilizing the interferometer directly on the phase relation between the pump and probe, we demonstrate a low temporal jitter of only 13 as. The setup was built to allow for several types of interferometric measurement schemes, such as RABBIT and KRAKEN.

I participated in the design and implementation of a new attosecond interferometer. I also participated in the measurements, and in the manuscript with comments and feedback.

Paper II: Influence of final state interactions in attosecond photoelectron interferometry

In this paper, we study the photoionization of argon atoms across the $3s^{-1}4p$ Fano resonance with high spectral-resolution RABBIT measurements. We find a large variation of the measured spectral phase depending on experimental conditions, such as the probe lasers bandwidth. We show that the phase in influenced by final state interactions.

I participated in the measurements, and in the manuscript with comments and feedback.

Paper III: Resonant two-photon ionization of helium atoms studied by attosecond interferometry

In this paper, we study resonant two-photon ionization via the 3p, 4p and 5p Rydberg states in helium. Using angle-resolved and angle-integrated Rainbow RABBIT measurements, we interpret the observed phase variations as a function of angle and energy using perturbation theory.

I participated in the measurements, and in the manuscript with comments and feedback.

Paper IV: Continuous-variable quantum state tomography of photoelectrons

In this paper, we propose a continuous variable quantum state tomography protocol of a photoelectron. With a bichromatic probe with phase-locked synchronized spectral components, we can couple different spectral parts of the photoelectron wave-packet to the same final energy. By scanning over the bichromatic frequency separation and the pump-probe delay, a sparse density matrix can readily be obtained. The KRAKEN method is tested numerically in the vicinity of Fano resonances in both helium and argon. A possibility to control the ion-photoelectron entanglement by varying the XUV bandwidth, is also presented.

I participated in the measurements, and in the manuscript with comments and feedback.

Paper V: Measuring the quantum state of photoelectrons

In this paper, we demonstrated the first KRAKEN measurements. We measure the density matrix of photoelectrons ionized in helium and argon. Comparisons with theoretical calculations showed excellent agreement.

I participated in the experiment design and the building of the experimental setup. I took a large part in the measurements and participated in the interpretation, the discussion of the results and writing of the manuscript.

Paper VI: Towards quantum-state tomography of photoelectrons using spectral Golomb rulers

In this paper, we demonstrate an improvement of the KRAKEN protocol. By using a Golomb ruler for the probe spectra, both the temporal- and frequency-domains can be utilized more efficiently. This allows for the retrieval of several sub-diagonals in a single measurement, thereby decreasing the time for an experiment.

I participated in the experiment design and the building of the experimental setup. I had the idea of how to successfully implement a polychromatic probe, with the optimal solution being a Golomb ruler. I took a large part in the measurements, in the interpretation, the discussion of the results and writing of the manuscript.

Appendix

Paper VII: A single-shot dispersion-scan based on a grism

In this paper, we present a single-shot d-scan technique using a prism combined with a grating (grism) to extend the dispersion range beyond the limit of a single prism. This allows measurement of longer pulses (25 fs FTL) and pulses with complex spectral phases without requiring larger beam sizes or additional dispersion compensation. The method is validated by comparison with conventional d-scan measurements.

I participated in the measurements, and in the manuscript with comments and feedback.